GEOLOGY 72H

DECEMBER 2016 • VOL 2

INSIDE:

GEOLOGY 72H

DECEMBER 2016 • VOLUME 2

The papers in this volume are the results of original research done by the students of Geol 72H, Field Geology of Eastern California, during the fall semester of 2016. This honors class is part of the First-Year Seminar program at the University of North Carolina at Chapel Hill. Beginning in 2009, students performed original research as part of this class, and this volume represents the second compilation of such research.

Field Geology of Eastern California is an expensive class, and we would like to thank all of those who have made this course possible. In particular, generous gifts from the Anadarko Petroleum Company have supported this class since its inception 15 years ago, and in recent years the Honors Program at UNC has contributed significant support. The Graduate Research Consultant Program the Office of Undergraduate Research and the Department of Geological Sciences both provided graduate student support so that the ratio of instructors to students is high.

I would like to particularly thank Prof. Drew Coleman, who joined the class as a second faculty member, graduate students John Boyd and Tyler Wickland, and undergraduate Emma Blackwell for providing excellent field instruction to the students as well as setting good examples for how research is done and how to thrive in the field. The Sierra Nevada Aquatic Research Laboratory and the White Mountain Research Station provided excellent base camps for our efforts, and we all are grateful to the staffs there for their help and hospitality.

—Allen Glazner, Professor of Geological Sciences and Geol 72H instructor, Fall 2016

Cover: Steeply tilted brown schist and gray marble at the former Pine Creek tungsten mine west of Bishop, California. Pine Creek was a leading producer of this strategic metal, important to the war effort in World War II. Photo by Jack Davidson.

Modeling geology with everyday technology: using 3-D imaging to determine the geologic origins of the Earthquake Fault near Mammoth Lakes, California

Taylor Weckstein, Megan Raisle, Ruth Tomlin, and Kaleb Lyda
Department of Geological Sciences, University of North Carolina, Chapel Hill, North Carolina 27599-3315, USA

ABSTRACT

Three kilometers northwest of Mammoth Lakes, California there is a crack known as the "Earthquake Fault" which is locally up to 20 m deep. The feature is located at the southern end of, and oriented parallel to, the Mono-Inyo Craters. It is mapped and popularly called a fault, but based on recent volcanic activity in the area and the lack of measured motion on the fault, it may actually be a volcanic fissure. To determine the degree of faulting and fissuring, points on both walls that showed evidence of strike-slip, dip-slip, or extensional movement were labeled. The points were then placed in a 3-D model; their relative positions were broken down into vector components to isolate extensional, dip-slip, and strike-slip movement. The crack exhibited significant extensional movement at both testing locations (1.34 m at location A and 2.11 m at location B). At location A the crack showed minimal right-lateral strike-slip movement and minimal normal dip-slip movement (0.12 m and 0.17 m). However, at location B the crack showed notable right-lateral strike-slip movement and notable normal dip-slip movement (0.90 m and 1.27 m). These data are consistent with a propagating dike, not tectonic movement, forming the fissure. Differences in local stress could account for different strike-slip and dip-slip movement. This makes the term *Earthquake Fault* a misnomer.

INTRODUCTION

Just outside of the popular ski town of Mammoth Lakes the National Forest Service advertises the Earthquake Fault, an impressive gorge locally up to 20 m deep (Fig. 1). Despite the potential hazards of a crevice located only 3 km northwest of Mammoth Lakes, how the feature formed is not well understood. Sharp and Glazner (1997, p. 255) discounted the likelihood of an origin by thermal contraction because the "host lava is too old . . . it is unlikely that open cracks could have survived for 50,000 years or more without filling with glacial debris, pumice from nearby eruptions, or loose rock". Furthermore, they ruled out a landslide origin based on local topography.

As the name suggests, the crevice may have opened due to faulting, a plausible explanation given recurrent tectonic activity in the region. The Earthquake Fault is situated along the eastern margin of the Sierra Nevada Range, where there are active strike-slip and normal faults due to the northwest translation of the Sierran microplate relative to the rest of North America (Unruh et al., 2003). The stress due to this translation could potentially be the cause of the Earthquake Fault (Bailey, 2004).

Others hypothesize the Earthquake Fault is related to magmatic, not tectonic, activity. The feature, located just south of the Inyo Craters, is part of an extensive system of faults and fissures that lie parallel to the Mono-Inyo volcano chain (Benioff and Gutenberg, 1939). Through the drilling of a slant hole between Obsidian Dome and Glass Creek Flow — two features located in the northern section of the Inyo chain— Eichelberger et al. (1985) encountered the dike that fed Obsidian Dome. Their findings suggest that episodic ascent of rhyolitic magma created explosive volcanism and fed the Inyo Craters 650-550 yr B.P. Due to the parallel alignment of the faults and fissures along the dike-fed Mono-Inyo Craters, Mastin and Pollard (1988) proposed that the pressure of a subsurface dike intrusion not only created the volcanic chain, but also created the related fissures and faults. Mastin and Pollard represented this subsurface dike intrusion using a flour and sugar model. Through their experiments, they found that fissures and faults formed both parallel to and directly above the model dike, similar to the situation along the Mono-Inyo system. Even though the dike did not penetrate to the surface everywhere, the pressure of the expanding magma could have caused inelastic deformation near the Earthquake Fault (Reches and Fink, 1998).

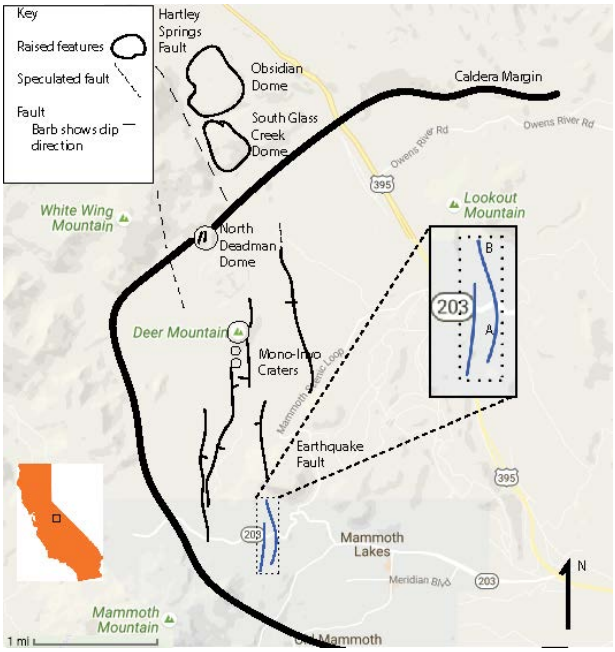

Figure 1: Faults and fissures of the Mono-Inyo region and their proximity to the town of Mammoth Lakes. Adapted from Reches and Fink, 1998.

Our research aims to synthesize these previous studies and determine the factors that contributed to formation of the Earthquake Fault using 3-D modeling and analysis. Significant strike-slip or dip-slip movement at the Earthquake Fault would suggest tectonic activity. However, we hypothesize the feature will exhibit primarily extensional opening above a subsurface dike intrusion. This information is pertinent to the safety of nearby residents and tourists given its potential association with future eruptions or earthquakes.

METHODS

We surveyed two relatively deep and well-exposed regions of the Earthquake Fault, location A to the south of Highway 203 and location B to its north (Fig. 1). At these locations we oriented the model on a grid system where the positive y-axis faces north, the positive x-axis faces east, and the positive z-axis shows elevation upward (Fig. 2). We created the grid using a TruPulse 360 laser rangefinder with an electronic compass to determine the coordinates of reference points relative to an arbitrary origin.

We photographed the east wall, west wall, and floor at both locations. We organized the pictures into "chunks" of approximately 60-100 photos each including at least one reference point. All adjacent segments overlapped by at least 60% to ensure accurate alignment of the chunks. We compiled the pictures in Agisoft PhotoScanPro (www.agisoft.com) to make 3-D models using the following workflow. We imported the pictures, one chunk at a time, into a new file. Then, before aligning the photos, we checked photo quality and eliminated any photos that were blurry. After the software aligned the photos we added coordinates to the markers on individual photos. To do this, we went to thereference pane, edited point names, set coordinate accuracy, switched to "local coordinates," entered (x,y,z) coordinates, and updated. Following

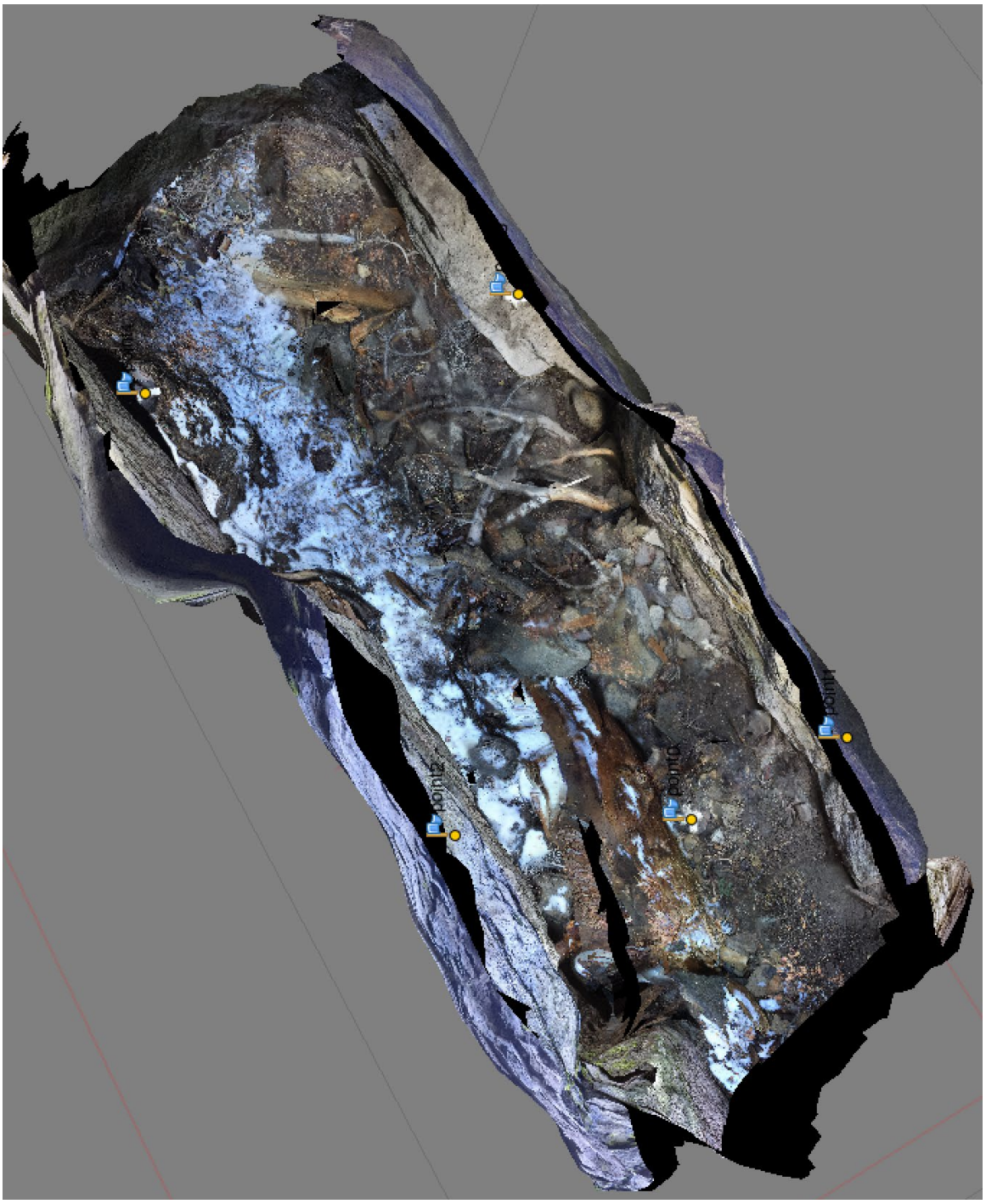

Figure 2: 3-D model looking vertically downward at location B of the Earthquake Fault.

this we built the dense point cloud, mesh, and texture (Fig. 3).

We used the models to estimate offset between the east and west walls. To calculate displacement vectors($\overrightarrow{D}$)we subtracted coordinates of piercing points (points that we infer were once connected) on the west wall ($\overrightarrow{pw}$) from coordinates of piercing points on the east wall ($\overrightarrow{pe}$). To represent extension we calculated the face normal vector ($\overrightarrow{N}$) near each piercing point using the cross product of two vectors ($\overrightarrow{v1}$ and $\overrightarrow{v2}$) on the face.

$$\overrightarrow{D} = \overrightarrow{pw} - \overrightarrow{pe}$$

$$\overrightarrow{N} = \frac{\overrightarrow{v1} \times \overrightarrow{v2}}{\left\| \overrightarrow{v1} \times \overrightarrow{v2} \right\|}$$

To compare these two vectors, we calculated the strike component, dip component and extension component at each location (Fig. 3). Furthermore, we found the trend and plunge of the face normal and displacement vectors, along with the angle between the displacement and face normal vectors. See supplemental data for detailed calculations.

RESULTS

The data indicate an average of 1.73 m of extension, an average of 0.51 m of right lateral strike-slip movement and an average of 0.72 m of east wall up, normal dip-slip movement at the Earthquake Fault (Table 1). Likewise, an average angle of 23° separates the displacement vector ($\overrightarrow{D}$) from the face normal vector ($\overrightarrow{N}$).

DISCUSSION

Both locations show extension as the largest component compared to dip-slip and strike slip components. Location A shows almost purely extensional opening; the strike-slip and dip-slip components are negligible. However, at location B the dip-slip and strike-slip components are a significant fraction of the extensional component. Had the Earthquake Fault been a result of tectonic movement, we would expect both locations to show similarly significant dip-slip and strike-slip components. On the contrary, as the Mono-Inyo dike swarm propagated toward the surface it may have released accumulated right-lateral elastic strain from northwest-trending eastern Sierran fault zone (Denlinger and Riley, 1984). Potential differences in the amount of elastic strain at each location may account for the discrepancy in dip-slip movement.

Furthermore, the data indicate 1.27 m of normal movement (east wall up) at location B. Mastin and Pollard (1988) conducted flour and sugar experiments that show that normal dip-slip movement can occur above a rising dike. They inserted a "dike" of two linoleum sheets into a "crust" of sugar and flour in order to model the pattern of faults and fissures along the Mono-Inyo Craters. Mastin and Pollard discovered a graben above the dike intrusion bounded by inward-facing normal faults similar to the findings at location B. Due to the episodic ascent of magma below the Earthquake Fault, certain areas may exhibit normal faulting while other areas exhibit negligible dip-slip movement (Eichelberger et al., 1985). Therefore, despite the discrepancy between strike-slip and dip-slip movement, we still hypothesize that mixed-mode extension from a subsurface dike intrusion, not tectonic movement, formed the Earthquake Fault.

Our results have direct implications regarding the safety of the nearby town of Mammoth Lakes. The town of Mammoth Lakes lies in an area characterized by crustal weakness, intersecting fault zones, and magma intrusion (Bailey, 2004). Although the main sections of the Earthquake Fault are 3 km away from the town, the feature extends into an area of development. If the Earthquake Fault is a result of a subsurface dike, the magma that feeds the dike could expand and cause surface eruptions (Sharp and Glazner, 1997).

Beside the Cascade Range in Washington and Oregon, the

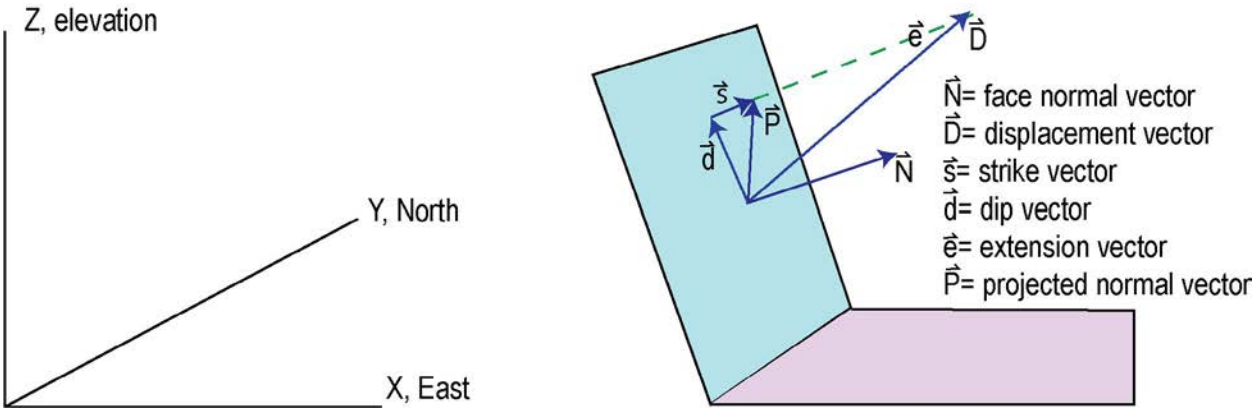

Figure 3: The orientation of the Earthquake Fault on our grid system and the relationship between the face normal vector, the displacement vector, and the strike, dip, and extension components.

Table 1. Measurements of offset between east and west walls at locations A and B. Positive strike indicates right-lateral movement and positive dip indicates normal movement (east wall up).

Calculated values from vector coordinates	Location A	Location B
Strike component	0.12 m	.90 m
Dip component	0.17 m	1.27 m
Extension component	1.34 m	2.11 m
Displacement vector plunge and trend	14° to 289°	8° to 280°
Face normal vector plunge and trend	19° to 289°	29° to 255°
Angle between displacement vector and face normal vector	9°	36°

area surrounding the Mono-Inyo Craters of eastern California exhibits more recent volcanism than anywhere else in the continental United States (Mastin and Pollard, 1988). Since 1979 the resurgent dome has expanded with approximately 0.3 km^3, of magma (Bailey, 2004). Although this relatively small influx of magma is unlikely to cause a large eruption, even a small eruption could be devastating to the town (Benioff and Gutenberg, 1939). Dike injection caused significant earthquakes in 1980 near Mammoth Lakes, and a further influx of magma could spur new, similar earthquakes (Bailey, 2004). It is impossible to predict if or when these events may occur, but town members and government officials should work with geologic experts to mitigate risk.

In addition to the direct implications of our research, our study shows how improving technology enhances geologic research. Cayol and Cornet (1998) used 3-D imaging technology to determine the geologic history of Piton de la Fournaise Volcano. Using photogrammetric surveys and displacement vectors, they discovered a dike that formed an *en echelon* pattern as it propagated toward the surface, feeding two destructive eruptions of the volcano. Together, our studies show that 3-D imaging and displacement vectors are effective tools to determine geologic origins and differentiate features such as fissures and faults.

The technology Cayol and Cornet used was cumbersome, slow, and expensive compared to modern technology. By using iPhones to take the high resolution photographs, we demonstrated the accessibility of modern technology as a means for geologic research. As technology proliferates and becomes increasingly accessible, more people will have the means to conduct geologic research. Moreover, this new age of 3-D modeling allows researchers to take the field into their computer and continue to produce novel data long after the field work is done. For example, we generated a virtual view of the Earthquake Fault that could only be directly photographed with great difficulty (Fig. 2).

CONCLUSIONS

Compared to the magnitude of extension at the Earthquake Fault, our data show relatively minimal dip-slip and strike-slip movement, especially at location A. Therefore, our findings support the hypothesis that primarily magmatic activity, not tectonic activity, formed the Earthquake Fault. The common name is misleading as the feature appears to be a fissure. However, the findings cannot directly prove that a dike intrusion created the Earthquake Fault. Rather, the research supports the hypothesis that tectonic activity in Owens Valley is not directly related to the feature. Further investigation is necessary to clarify discrepancies in our data and fully determine the origin and potential implications of the Earthquake Fault. Either way, our experiment shows the efficacy of 3-D modeling for geologic analysis, and the benefits of modern research approaches. There are also serious safety implications for residents and visitors of Mammoth Lakes. Potential earthquakes or eruptions from an influx of magma underneath the Earthquake Fault could cause substantial destruction. The community of Mammoth Lakes should continue to monitor the area for signs of magmatic activity.

ACKNOWLEDGMENTS

This research was supported by the Department of Geological Sciences at the University of North Carolina at Chapel Hill, the Anadarko Petroleum Corporation, the UNC Honors Program, the First-Year Seminar Program, the Office of Undergraduate Research Graduate Research Consultant Program, and the staffs of the Sierra Nevada Aquatic Research Laboratory and Crooked Creek Station of the White Mountain Research Center. We would like to extend special thanks to Dr. Allen Glazner for making our trip to California possible, for accepting the death of his computer with utmost grace and kindness, for his assistance and leadership in the field, for the hours of troubleshooting Agisoft with us, and for (sometimes) being our friend. Also special thanks to Dr. Drew Coleman for his utterly truthful and beautifully dry sense of humor in the field and the classroom; Tyler Wickland for allowing us to control the radio, being our cool friend, and being wicked smart and passionate about geology; Emma Blackwell for being a beautiful human and helping us with calculus; John Boyd for always lending a helping hand; Dr. Kevin Stuart for always being willing to consult with us; the Agisoft support team for answering our inquiries promptly and with care; Ashley Meise for offering a much-needed hand in the field and back at home; Cecil, Scooter, Scottie, Steven, and everyone at SNARL and Crooked Creek that allowed us to have such a splendid place to stay; everyone in Geology 72H; and finally, each other for putting together a great team.

REFERENCES CITED

2016, Agisoft PhotoscanPro v. 1.2.6 for macintosh: www.agisoft.com.

Bailey, Roy A., 2004, Eruptive history and chemical evolution of the precaldera and postcaldera basalt dacite sequences, Long Valley, California; implications for magma sources, current seismic unrest, and future volcanism: U.S. Geological Survey Professional Paper 1692, 75 p.

Benioff, H., and Gutenberg, B., 1939, The Mammoth "Earthquake Fault" and related features in Mono County, California: Bulletin of the Seismological Society of America, v. 29, p. 333-340.

Cayol, V, and Cornet, F, 1998, Three-dimensional modeling of the 1983-1984 eruption at Piton de la Fournaise Volcano, Réunion Island: Journal of Geophysical Research, v. 103, p. 18025–18037, doi:10.1029/98JB00201.

Denlinger R.P., Riley F, 1984, Deformation of Long Valley Caldera, Mono County, California, from 1975 to 1982: Journal of Geophysical Research, v. 89, p. 8303–8314, doi:10.1029/JB089iB10p08303.

Eichelberger, J. C., P. C. Lysne, C. D. Miller, and L. W. Younker, 1985, Research drilling at Inyo domes, California: 1984 results: Eos Trans. AGU Publications, v. 66, p 186–187, doi:10.1029/EO066i017p00186.

Mastin, L.G., and Pollard, D.D., 1988, Surface deformation and shallow dike intrusion processes at Inyo Craters, Long Valley, California: Journal of Geophysical Research, v. 93, p 13221–13235, doi:10.1029/JB093iB11p13221.

Reches Z. and Fink J, 1998, The mechanism of intrusion of the Inyo Dike, Long Valley Caldera, California: Journal of Geophysical Research, v. 93, p. 4321–4334, doi: 10.1029/JB093iB05p04321.

Sharp, R.P., and Glazner, A.F., 1997, Geology Underfoot in Death and Owens Valley, Mountain Press Pub., 319 p. 255.

Unruh, J., Humphrey, J., and Barron, A., 2003, Transtensional model for the Sierra Nevada frontal fault system, eastern California: Geology (Boulder), v. 31, p 327–330, doi:10.1130/0091-7613(2003)031.

Using Google Earth to aid in the study of jointing in the Sage Hen Flat pluton, White Mountains, California

Ashley Meise, Patton Orr, and Hannah Smith
Department of Geological Sciences, University of North Carolina, Chapel Hill, North Carolina 27599-3315, USA

ABSTRACT

We evaluated Google Earth as a tool for collecting azimuths of steep joints in rocks through comparison of field data collected from the Sage Hen Flat pluton, White Mountains, California with data collected in the same area via Google Earth. Rose diagrams created with data obtained through by different methods are strikingly similar. Our data indicate that Google Earth is a viable method for collecting data and is especially useful for surveying field locations before arrival. As the program allows one to see prominent joint patterns from above, Google Earth makes it easier for one to know what to look for when in the field; however, Google Earth does not eliminate the necessity of actually going to the field to collect data as one can only plot vertical joints and dip data are impossible to collect.

INTRODUCTION

Google Earth is an online visual geographical database produced by Google, depicting satellite imagery on a virtual globe. Through the use of the ruler tool, land surface trends such as fault or fracture line orientations can be obtained directly (Putchner, 2011). We addressed the reliability of using Google Earth as an option for collecting joint azimuths by comparing field data collected on the Sage Hen Flat pluton in eastern California with data collected in the same area with Google Earth. Through the use of rose diagrams, we are able to see the relative frequency of azimuths, allowing for a direct comparison of Google Earth data to field data. Furthermore, we examined the potential causes of joint patterns present in the pluton.

BACKGROUND

The Sage Hen Flat pluton is an isolated Middle Jurassic granite body in the White Mountains of eastern California that covers a roughly circular area of 17 km^2. The pluton was dated by the U-Pb method on ziron at 175 Ma (Coleman et al., 2003). The following geologic history is taken from Nelson et al. (1991). The pluton is unique in the area because the country rock shows little evidence of deformation by forcible emplacement. The early and middle Cenozoic was a time of large-scale uplift and extensive erosion, and a major erosion surface cuts all previously formed rocks in the area. The late Cenozoic was a time of renewed uplift along Basin and Range normal faults flanking the range, and strike-slip motion occurred along the Furnace Creek fault zone at the margin of the White Mountains and Fish Lake Valley. Both events reflect major episodes of crustal extension initiated in the Basin and Range Province about 15 million years ago. This deformation continues to the present in the White-Inyo region.

Joints in the Sage Hen Flat pluton are important to study as they are clearly visible and there are multiple sets in each outcrop. Due to the visibility of the joints, it is easier to decipher the prominent joint patterns in the area, allowing one to make inferences about potential regional stresses. Furthermore, the prominence of these joints, and the lack of vegetation in the area, helps to increase how much one can discern from a satellite image, making this pluton an ideal location to study when assessing the merits of using Google Earth to measure joint azimuths.

METHODS

We measured joint attitudes in 14 different outcrops in the northwestern quadrant of the Sage Hen Flat pluton, selecting outcrops that appeared to be in place (Figs. 1-3). We recorded our location by taking photographs of each outcrop on an iPhone camera and importing the location data into one map. At each outcrop (Fig. 4), we measured the strike and dip of dominant joint sets and faults using a Brunton compass. Faults were recognized by slickensides on the granite. We collected 99 joint orientations and 7 fault orientations, measuring both steep and flat joints.

Using Google Earth, we measured an additional 267 joint azimuths (photolineations). From satellite imagery we could clearly see prominent joint sets in outcrops on Sage Hen Flat. We chose to use imagery from 2012 because the images were taken at a time of day where there were relatively few shadows, giving

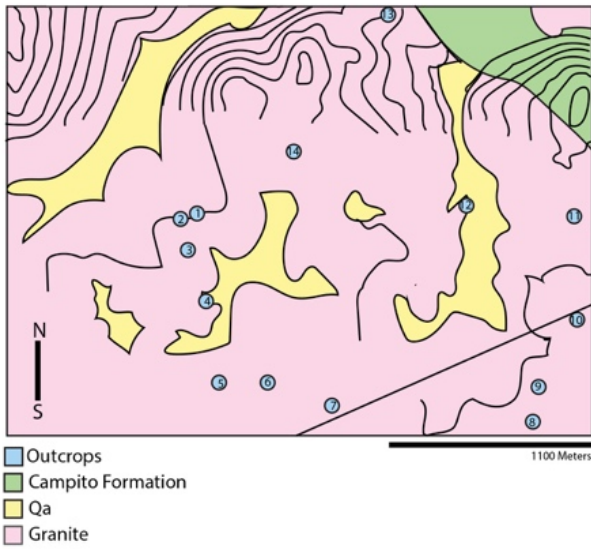

Figure 1. Geological map of the Sage Hen flat showing 14 outcrops, labeled in the order we mapped in.

Figure 2. Picture from Google Earth showing a classic outcrop demonstrating two prominent joint sets.

Figure 3. Map showing the location of the Sage Hen Flat pluton in California.

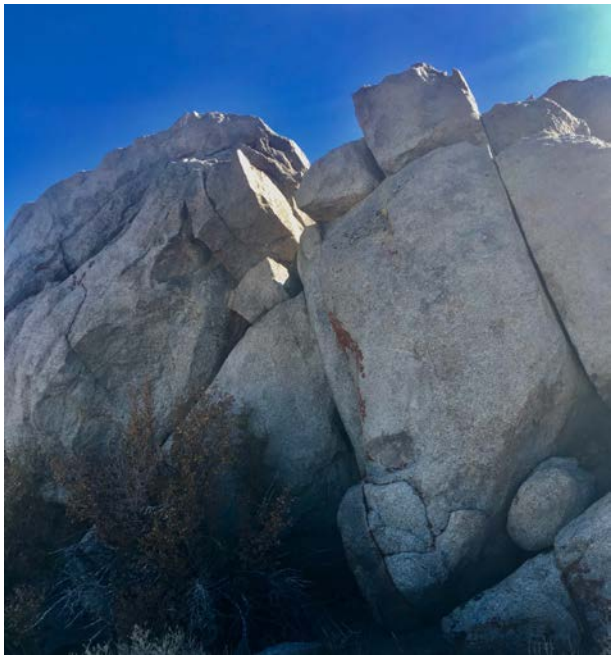

Figure 4. A picture taken of Outcrop 4, showing prominent steep joints.

us the clearest view of the joints (Fig. 2). Measurements could only be taken from steep joints, as we were unable to see shallow joints from satellite imagery. Using Google Earth, we recorded joint measurements in the area we covered in the field and outside it. By adding a 2-point path along these joints in Google Earth, we were able to obtain the azimuths. The kml file containing the line segments was parsed in Matlab using the function getElementsByTagName and the starting and ending latitudes and longitudes were extracted. An azimuth was calculated from these end points using the following formula for forward azimuth:

$$\theta = \text{atan2}(\sin\Delta\lambda \cdot \cos\varphi 2, \cos\varphi 1 \cdot \sin\varphi 2 - \sin\varphi 1 \cdot \cos\varphi 2 \cdot \cos\Delta\lambda)$$

where φ is latitude and λ is longitude. The function atan2 returns the arctangent of the specified x- and y-coordinates using two arguments, giving the quadrant the angle is located in. The angle is given in radians between -π and π, excluding -π (Veness, 2016). Using Stereonet 9 by Rick Allmendinger, we plotted the poles of the strike and dip directions measured in the field, finding five different joint sets. We also used the program to create rose diagrams of our field data and Google Earth data (Figs. 5-7). With a combination of images from Google Earth, pictures taken in the field, and a digitally constructed model of outcrop 7 made with PhotoScan (www.agisoft.com), we estimated the approximate order in which different joint sets formed.

RESULTS

Field data show that there are two perpendicular joint sets present in addition to a shallow joint set in the northern part of the mapped area (Fig. 8). Measured faults were mostly shallow with irregular strikes (Fig. 9). Nearly all fault surfaces contain epidote. Faults were recognized in the field due to the presence of slickensides on the granite. Most joints had dips greater than 60°, excluding the shallow joint set measured in the northern part of the mapped region. The joints that strike northeast are generally more throughgoing than the joints striking northwest, making the joints that strike northeast the oldest of the two sets. The prominence of the northeast-striking joints is shown in both field and satellite images (Fig. 10). Figures 6 and 7 show striking agreement between field and remote sensing measurements.

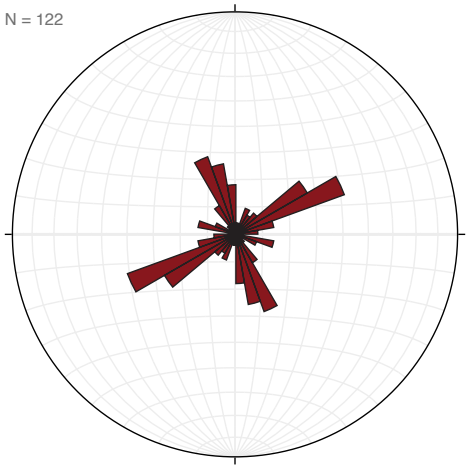

Figure 5. Rose diagram of azimuths measured with Google Earth, but only those located within the area of the pluton mapped in the field. The length of each petal represents the frequency of that azimuth measured.

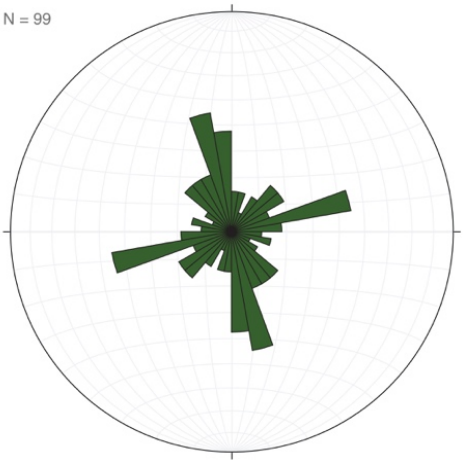

Figure 6. Rose diagram of azimuths physically measured in the field. The length of each petal represents the frequency of that azimuth measured.

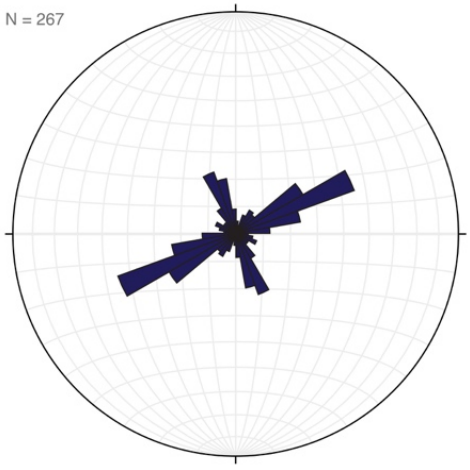

Figure 7. Rose diagram of all azimuths measured using Google Earth, including measurements taken outside of the area of the pluton not physically mapped. The length of each petal represents the frequency of that azimuth measured.

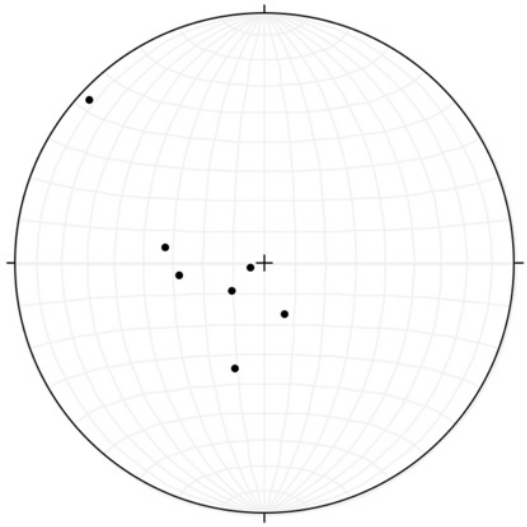

Figure 8. Stereonet of the poles of the faults.

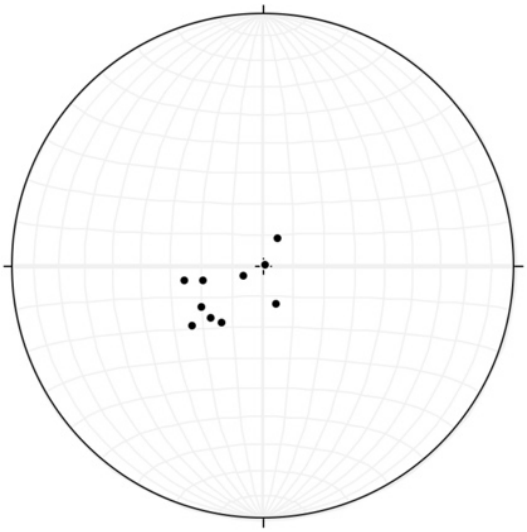

Figure 9. Stereonet of the poles of the low-angle joints.

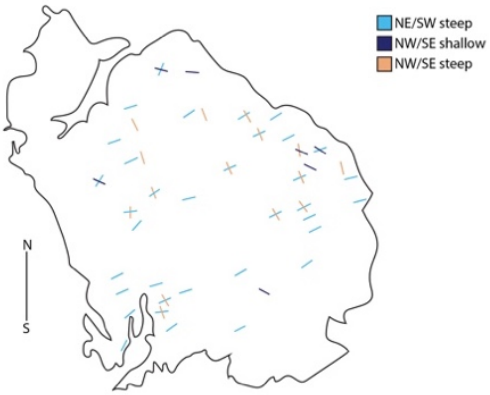

Figure 10. Map of Sage Hen Flat pluton showing color-coded joints mapped found using Google Earth. Light blue refers to primarily NE/SW joints, dark blue refers to shallow NW/SE joints and orange refers to steeper NW/SE joints.

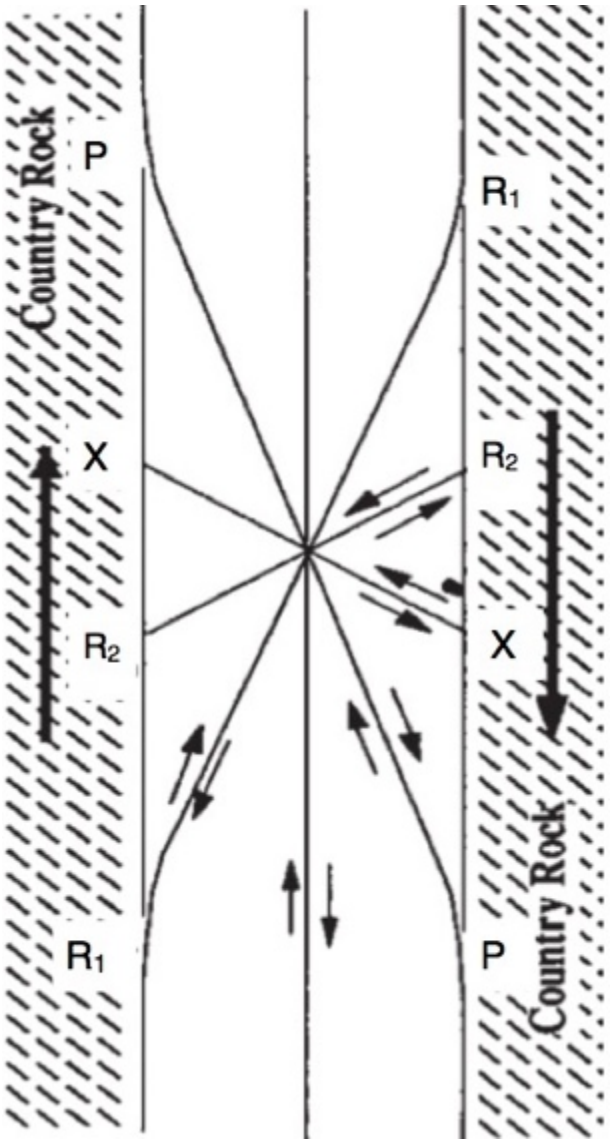

Figure 11: Diagram showing Riedel fracture patterns in a right-lateral shear zone. Adapted from Logan (2007).

DISCUSSION

The agreement between field and remote sensing measurements of the orientations of steep joints (Figs. 6,7) indicate that Google Earth can be an important adjunct to field data. In a relatively short amount of time, we were able to take roughly 270 measurements of joints from 150 outcrops spanning the entirety of the pluton. In comparison, it took eight hours to collect around 120 measurements from only 14 outcrops when in the field. Furthermore, collecting joint azimuth data on Google Earth allowed us to quickly see and understand developing patterns (the two distinct joint sets), something that was more difficult to pick up on while in the field. Therefore, we see Google Earth as a useful resource for understanding and surveying local geology *both* before and after field research. By plotting the azimuths of hundreds of joints, one can arrive at a statistically clear idea concerning the nature of an area's joint sets. Nevertheless, limitations of such an approach still exist—satellite imagery must be sufficient in terms of resolution, on cannot plot shallowly dipping joints, and dip data are impossible to collect.

Satellite imagery is useful beyond simply plotting joint azimuths. It can help one determine the primary joint set in an area, which can be judged through two criteria—which joint

set is most throughgoing, and which set is most numerous. Through satellite imagery one can visualize the termination of one joint into another and crosscutting relationships. Furthermore, one can see how joint orientations fit into the broader geologic landscape of an area. When looking at the Sage Hen Flat pluton on Google Earth, we spotted a series of valleys that run roughly parallel to Joint Set B (marked on Fig. 5). That these ridges run perpendicular to the primary joint set is somewhat peculiar, and a better understanding of regional stress and erosion history would aid in attempting to explain this anomaly. Jointing in granitic plutons is caused by regional tectonic stress or internal stress caused by cooling, or some combination thereof (Bergbauer and Martel, 1999). The consistency of the joint orientations across the entire pluton (Fig. 10) suggests that regional stress caused jointing in the Sage Hen pluton, because joints caused by cooling stress are generally radial (Bergbauer and Martel, 1999). Although there are few faults within the pluton itself (Bilodeau, 1981), Cenozoic right-lateral strike-slip faults on either side of the White Mountain range mapped by Stockli et al. (2003) could be responsible for joint formation in the pluton. In such a shear zone, the joints could have formed along Riedel shears. The lack of noticeable R_1 fractures (Fig. 11) within the pluton seems to conflict with this argument, although there is the possibility that the pluton has rotated since the joints formed, deviating what could have potentially been R_1 fractures to their present-day orientations. Furthermore, the varied composition of the White Mountains could have altered the direction of the assumed north/south regional stress, causing the Riedel shears to propagate in different orientations. Whereas most research about the White Mountain shear zone focuses on the more recent (< 10 Ma.) strike-slip activity, there is the possibility that older dip-slip tectonics created the regional stress responsible for the joints seen today.

CONCLUSION

Photolineations imaged with Google Earth provide a useful source of data concerning orientations of major joint sets within a pluton. Satellite imagery also provides a means to view local geography though a macroscopic context. Though the origin of our two joint sets is inclusive, regional stress was the most likely contributing factor. Further field research—including paleomagnetism, microfault analysis, and mineral analysis—could shed light into this question.

ACKNOWLEDGMENTS

This research was supported by the Department of Geological Sciences at the University of North Carolina at Chapel Hill, the Anadarko Petroleum Corporation, the UNC Honors Program, the First-Year Seminar Program, the Office of Undergraduate Research Graduate Research Consultant Program, and the staffs of the Sierra Nevada Aquatic Research Laboratory. We would like to extend special thanks to Dr. Allen Glazner for his ingenuity in coming up with not only one backup project, but two. Additionally, we would like to thank him for his willingness to drive us around California for a week, getting us where we needed to be in record time. We would also like to thank Dr. Drew Coleman for his sunny disposition both in the classroom and in the field, John Boyd for his constant help with our many, many questions, Emma Blackwell for her tireless support, and finally, Tyler Wickland for his patience with us in the lab and for allowing us to take food breaks at Cosmic Cantina.

REFERENCES CITED

Allmendinger, R. W., 2016, Stereonet 9, v. 9.8.6 X for Macintosh: http://www.geo.cornell.edu/geology/faculty/rwa/programs/

Bergbauer, S. and Martel, S.,1999, Formation of joints in cooling plutons. Journal of Structural Geology 21. P. 821-835.

Bilodeau, B. J., 1981, Structure and Emplacement of the Sage Hen Flat Pluton, White Mountains, California [MS.]: University of California Los Angeles.

Bilodeau, B. J., and Nelson, C. A. 1993. Geology of the Sage Hen Flat pluton, White Mountains,

California. Geological Society of America Map and Chart Series MCH077, scale 1:24,000.

Coleman, D. S., Briggs, S., Glazner, A. F., and Northrup, C. J., 2003, Timing of plutonism and deformation in the White Mountains of eastern California: Geological Society of America Bulletin, v. 115, p. 48-57.

Logan, J.M., 2007, The progression from damage to localization of displacement observed in laboratory testing of Porous Rock. The Relationship Between Damage and Localization. Ed. Lewis, H. & Couples, G. D., Geological Society, London, Special Publications, 289, P. 75-97.

Nelson, C. A., Hall C. A. Jr., and Ernst W.A., 1991, Geologic history of the White-Inyo range, p. 42-74, In C.

Hall Jr. [ed.], Natural history of the White-Inyo range eastern California. Univ. Calif. Press, Berkley, CA.

Putchner, R., 2011, Using Google Earth in Geotechnical Investigations: Magazine of the South African Institution of Civil Engineering, v. 19. p. 21-25.

Stockli, D. F., Dumitru, T. A., McWilliams, M. O., and Farley, K.A., 2003, Cenozoic Tectonic Evolution of the White Mountains, California and Nevada. GSA Bulletin, v. 115, p. 788-816.

Veness, C., 2016, Calculate distance, bearing and more between Latitude/Longitude points: http://www.movable-type.co.uk/scripts/latlong.html

2016, Agisoft photoscan pro 1.2.6

Evaluation of two competing hypotheses for contact relations of the Sage Hen Flat pluton, White Mountains, eastern California

Lizzie D. Wilson, Jed D. Higdon, and Jack A. Davidson
Department of Geological Sciences, University of North Carolina, Chapel Hill, North Carolina 27599-3315, USA

ABSTRACT

There are two different interpretations of the contact relations of the Sage Hen Flat pluton, an isolated Jurassic granite in the White Mountains of eastern California. Ernst and Hall (1987) mapped the northwestern contact as a relatively straight fault, whereas Bilodeau and Nelson (1993) interpreted the contact as intrusive. To investigate these two interpretations, we mapped the contacts and collected samples of the pluton and its wall rocks. We observed granite dikes cutting the Deep Spring Formation at the contact, which indicates intrusion, and did not find any offset contacts to corroborate the faulting hypothesis. We then analyzed the samples for grain size and Sr isotope ratios to determine whether the pluton had thermal or hydrothermal interactions with the metamorphic wall rock. Wall rock grain sizes coarsen toward the pluton contact. Crystal coarsening in Deep Spring Formation limestone as the contact is approached suggests recrystallization by the added heat of a cooling plutonic body. Consistent with this, our samples of granite contain smaller crystals near the contact and larger crystals away, suggesting that the rock at the contact crystallized more rapidly as it gave up heat and fluid. Our $^{87}Sr/^{86}Sr$ data support intrusion as well. Sr isotopic data from the wall rocks follow a typical mixing trend, consistent with fluid exchange between the pluton and its wall rocks. Our evidence supports the Bilodeau and Nelson interpretation of the area, in which the contact between the northwest side of the Sage Hen Flat pluton and the surrounding rock is a complex intrusive contact, rather than a fault.

INTRODUCTION

The Sage Hen Flat pluton in the White Mountains of California (Fig. 1) is a classic example of "cookie-cutter" emplacement, where metasedimentary strata appear to be chopped off at the pluton contact (Coleman, et al. 2005). The Late Proterozoic Deep Spring Formation borders the northwestern side of the Sage Hen Flat pluton (Fig. 1) and includes several different carbonates, as well as fine-grained orange and brown sandstone, skarn, and shale. The Sage Hen Flat pluton is much younger than the surrounding carbonates, with a U-Pb zircon age of ~175 m.y. (Coleman et al. 2003). It has been mapped three times (Nelson, 1966; Ernst and Hall, 1987; Bilodeau and Nelson, 1993). Although these maps are broadly similar, interpretation of the contact on the northwestern side of the pluton is controversial. Bilodeau and Nelson, following Nelson, interpreted this area as a complex intrusive contact (Fig. 2a), whereas Ernst and Hall mapped it as a fairly simple fault (Fig. 2b).

These two interpretations have significantly different implications for emplacement of the pluton and for its effects upon the wall rock. If the contact is intrusive, then we should expect changes in crystal size in both the wall rocks and pluton: coarsening of wall rock carbonates approaching the contact due to recrystallization, and fining of the pluton toward the contact due to chilling. If the contact is a simple fault, we should not expect to see any dramatic changes in the texture of either the carbonates or the pluton. We should also expect to find evidence of fluid exchange at an intrusive contact using Sr isotope analysis. ^{87}Sr is radiogenic, and is derived from ^{87}Rb, whereas the concentration

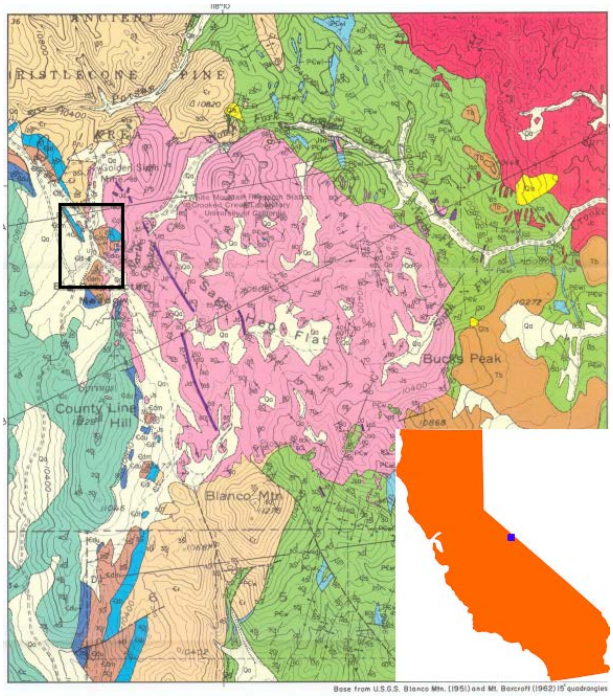

Figure 1. Section of the Blanco Mountain 15' quadrangle in the White Mountains of California with relative location in California. The Sage Hen Flat pluton is the pink ovoid formation in the center. We examined the northwest contact between the pluton and the Deep Spring Formation in the square pictured (Bilodeau and Nelson 1993).

of ^{86}Sr in the Earth is constant. Therefore, as rocks age, $^{87}Sr/^{86}Sr$ increases. Unaffected Deep Spring limestone has $^{87}Sr/^{86}Sr$ of ~0.7135, whereas the Sage Hen Flat pluton has $^{87}Sr/^{86}Sr$ of ~0.705 to 0.706 (D. Coleman, personal communication, 2016). Fluid exchange between limestone and granite should cause the affected limestone to have much lower $^{87}Sr/^{86}Sr$ than unaffected limestone. If the contact is intrusive rather than faulted, the data should reflect a hyperbolic mixing model. In order to decide which interpretation of the contact is valid, we examined the contact, studied crystal size at varying distances from the contact, and analyzed the isotopic composition of the carbonates.

METHODS

Mapping and Sample Collection

We collected samples from both the pluton and the wall rock from both far from and near to the contact to determine if such fluid exchange and grain size patterns exist. We also mapped the pluton contact for evidence of faulting or intrusion. We collected 22 samples of dolomite, limestone, granite, sandstone, and skarn from outcrops both far from and near to the contact between the Deep Spring Formation and the pluton (Fig. 3). We used the dolomite, limestone, and granite to compare relative contact metamorphism and grain size to distance from the contact; we used all seven limestone samples to compare their $^{87}Sr/^{86}Sr$ to that of a calculated hyperbolic fluid mixing model.

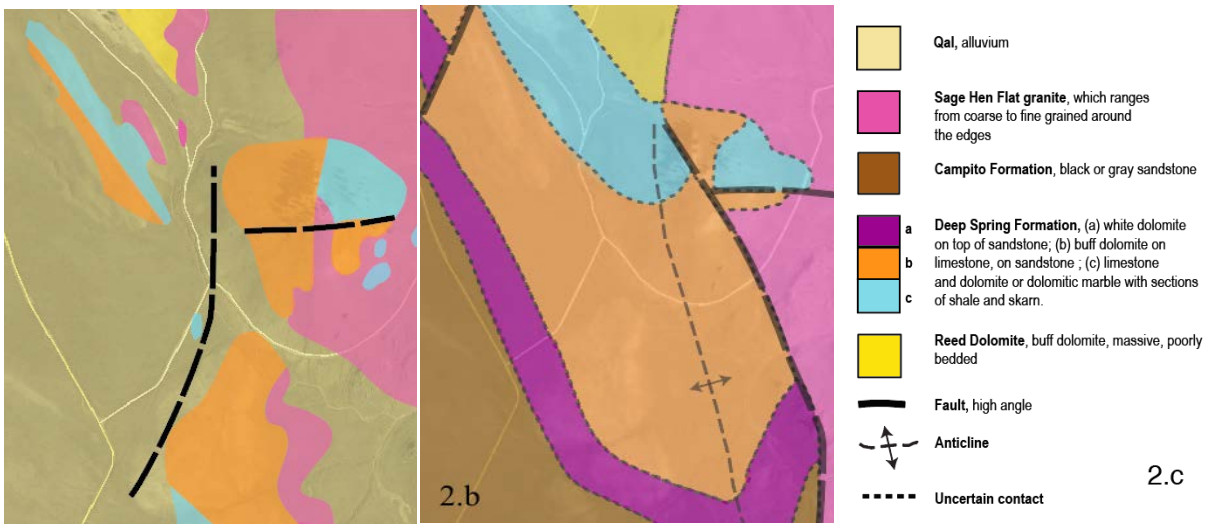

Figure 2. (a) Simplified version of the map created by Bilodeau and Nelson (a) in which the contact with the pluton is intrusive (Bilodeau and Nelson 1993). (b) Simplified version of the map created by Ernst and Hall in which the contact is a simple straight fault rather than an intrusion (Ernst and Hall 1987). (c) Composite stratigraphic key to the two maps above.

Sr Isotopic Analysis

We ran columns on 7 samples of Deep Spring limestone: 05, 12, 13, 14, 15, 16, and 17. The first five samples were taken from outcrops close to the contact with the pluton, in the central clump of samples (Fig. 3). Samples 16 and 17 were a greater distance away from the pluton; sample 16 was vertically far from the pluton relative to other samples, as it was on top of the central hill and sample 17 was horizontally far from the pluton (Fig. 3). The samples were crushed to roughly 2 mm chips. Several (5-15) mg of each samples was put into separate 7 mL Savillex beakers. The samples were dissolved in 525 μL of 3.5 M HNO3 and spiked with ^{84}Sr tracer. We isolated the Sr using Sr-SpecTM resin following standard University of North Carolina at Chapel Hill Department of Geological Sciences protocol. One drop of 1.00 M H3PO4 was added to the samples and they were evaporated to dryness. Samples were then loaded onto single Re filaments, and, using TaF_5, evaporated again to dryness. The samples were loaded into a VG-Sector-54 thermal ionization mass spectrometer, housed in the Geological Sciences building at the University of North Carolina at Chapel Hill. The samples were analyzed in triple dynamic mode with ^{88}Sr=3V using 10-11 Ω resistors and then corrected for mass fractionation, assuming $^{86}Sr/^{88}Sr$= 0.11940 and exponential fractionation behavior. Replicate analyses of NBS-987 yield $^{87}Sr/^{86}Sr$ = 0.710269 ± .000015 (2σ). We calculated concentration in ppm of Sr and plotted ppm Sr vs. $^{87}Sr/^{86}Sr$ to compare our data to a hyperbolic mixing model (Faure, 1986).

Crystal Size

To quantify crystal sizes, samples from both near to and far from the contact were mounted in epoxy in 1 inch rounds and cut so that an open plane of the rock was exposed. Using a Struers LaboPol-5 polisher, the samples were polished down to a 1 micron grit. Both the samples and polisher were washed and sonicated using soapy distilled water and distilled water in between grits. The samples were photographed at 100x magnification with an Olympus reflected light microscope. A polarizing lens was used to increase the contrast between crystals. The granite grain size is large enough to observe without the microscope; this round was photographed using a scanner. The crystal sizes were then hand measured on ImageJ. The greatest distance across each crystal was taken and mean crystal size was compared to the sample's distance from the contact. Each sample's location was plotted on Google Earth and a straight line was drawn between each sample and the nearest contact with granite. This distance was measured with the program's ruler tool.

RESULTS

Mapping

Offset contacts were found while mapping the area. One of the offset contacts is perpendicular to the pluton's contact with the wall rock, and despite being in the disputed area, it does not separate the granite from the wall rock. Rather, the offset is within the sandstone and dolomite (Fig. 2). Another key observation was that multiple granite dikes cut the wall rock at the contact (Fig. 4).

Figure 3. Sample locations in relation to the granite contact.

Figure 4. A granite dike intruding through the sandstone at the contact.

Strontium

$^{87}Sr/^{86}Sr$ plotted against Sr concentration closely follows the Sr fluid exchange model (Fig. 5). The end members were derived from the extremes of our $^{87}Sr/^{86}Sr$ data set. Samples 16 and 17 experienced the least fluid exchange, their $^{87}Sr/^{86}Sr$ close to the limestone end member (Fig. 5). The other 5 samples experienced much greater fluid exchange, their $^{87}Sr/^{86}Sr$ altered heavily by the low $^{87}Sr/^{86}Sr$ of the pluton. Sample 14, the one outlier of the data set marked in green, was skarn rather than limestone (Fig. 5).

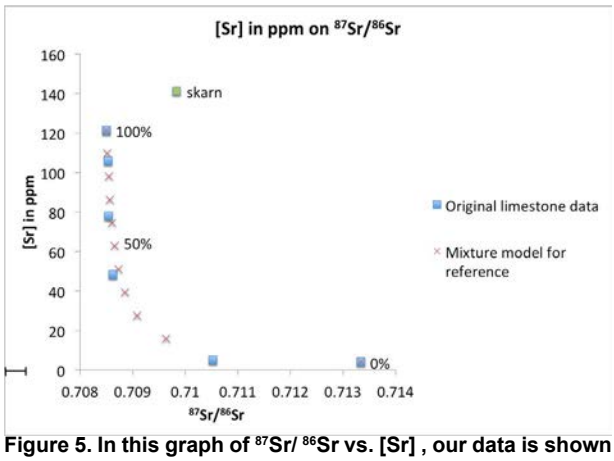

Figure 5. In this graph of $^{87}Sr/^{86}Sr$ vs. [Sr] , our data is shown as blue squares and the mixing model is shown as red Xs. When we used the extreme values as end members, ¬the remaining 4 limestone samples fall on a hyperbolic curve (Faure, 1986).The green square represents the sample of skarn, 14. The bar on the left side of the x-axis represents the 87Sr/86Sr of the Sage Hen Flat pluton of 0.705 – 0.706 (D. Coleman, personal communication, 2016).

Crystal Size

Crystal size data are consistent with an intrusive origin for the contact (Fig. 6). Limestone samples 16 and 12, less than 30 m from the contact with granite, have much larger crystal size that that of sample 17, which is over 500 m from the contact (Table 1). The dolomite's average crystal size in samples 07 and 08, less than 80 m away from the contact with granite, also had much larger average crystal size than sample 22, which was 8000 m away from the contact (Table 1). The average granite crystal sizes in 10, which was directly on the contact with the surrounding carbonates, were smaller than 21, which was 50 m away from the contact (Table 1). In Figures 7 and 8, the crystals at 100x magnification are larger in both the limestone and the dolomite near the contact than they are away from the contact. In Figure 9, the crystals in granite sample 10, directly at the contact, are much smaller than in those of sample 21, nearly 50 m from the contact (Fig. 9).

Sample Type/ Number	Distance from Granite Contact (m)	Average Crystal Size (mm)
Dolomite		
CC1607	20	0.209
CC1608	80	0.299
CC1622	8,000	0.101
Limestone		
CC1614	10	0.578
CC1616	30	0.264
CC1612	32	0.302
CC1617	565	0.175
Granite		
CC1610	0	0.769
CC1621	50	1.716

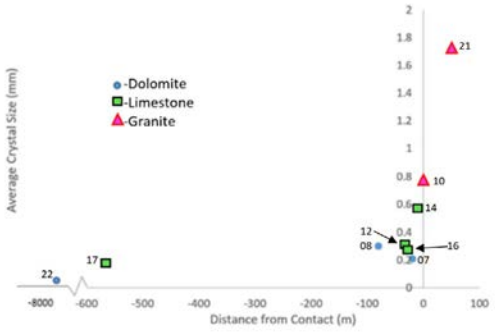

Figure 6. Dolomite, limestone, and granite average crystal sizes plotted against their distance from the contact. The carbonates that have larger crystal size are generally closer to the contact, whereas the opposite is true of granite.

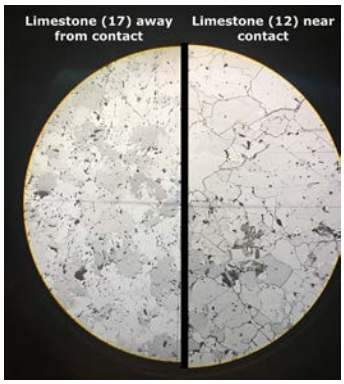

Figure 7. Polished limestone far and near the contact at 100x magnification. Sample 12 (right) and sample 17 (left).

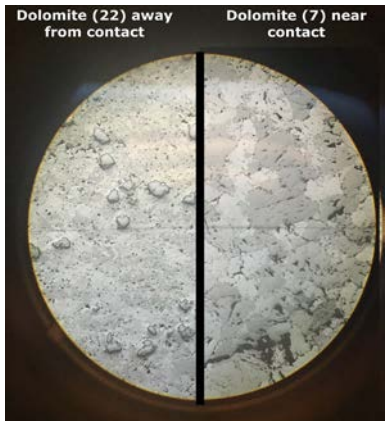

Figure 8. Polished dolomite far from and near to the contact at 100x magnification. Sample 07 (right) and 22 (left).

Figure 9. Polished granite far and near the contact at 100x magnification. Sample 21 (top right) and 10 (bottom left).

DISCUSSION

Trends

Our data's close conformity to the hyperbolic Sr fluid mixing model corroborates the crystal size data (Fig. 5). The fluid composition of the limestone was severely altered, an effect typical of complex intrusive contacts. This pattern of data is in line with the interpretation of the contact proposed by Bilodeau and Nelson (1993), as fluid exchange would not have occurred if the contact between the pluton and the carbonates were a simple fault. The carbonates experienced a net increase in crystal size with proximity to the contact with granite, whereas the granite experienced a net decrease in crystal size with proximity to the contact (Fig. 6). The significant changes in rock texture, from coarsening to fining, can be attributed to large heat changes within the region and contact metamorphism. The trend in crystal size in the carbonates and in the granite reflects typical behavior of wall rock and plutonic rock near an intrusive contact, and corresponds well with the interpretation of the contact proposed by Bilodeau and Nelson (1993). Our discovering a granite dike in the sandstone further suggests intrusion and potential for fluid exchange.

Anomalies

We saw a fairly consistent trend of increasing crystal size with proximity to the pluton within the carbonates, but it is important to note the slight differences. In dolomite, the sample 08 is 60 m farther from the contact than 07, but sample 8's average crystal size is larger. This anomaly is also present within limestone; sample 12 is about 2.5 m farther from the contact than sample 16, but sample 12's average crystal size is larger (Fig. 5). This does not change the integrity of our assertions because the crystal size difference and distances are small within the context, and the overall trend is not impacted. This anomaly is due in part to the way in which plutons are intruded. The contact between the granite and the carbonates does not extend straight down into the ground, but rather, it is likely that the pluton extends underneath the carbonates in places we cannot see or measure. For instance, the samples we deemed to be 80 m from the contact might in fact only be 10 m away because the pluton is directly underneath the outcrop. This means that the heat from the pluton coarsened carbonates farther from the visible contact than we would expect.

In the Sr study, there was one outlier in the data set, sample 14 (Fig. 4). This sample was retroactively determined to be skarn rather than limestone. Skarn should not react to fluid exchange in the same manner as limestone as it has different composition and properties. Therefore, sample 14's deviation from the other data is expected. There was also a discrepancy between the $^{87}Sr/^{86}Sr$ of limestone samples that experienced great fluid exchange and the natural $^{87}Sr/^{86}Sr$ of the Sage Hen Flat pluton. The smallest $^{87}Sr/^{86}Sr$ in our data was ~0.7085 (Fig. 4), whereas the original $^{87}Sr/^{86}Sr$ of the pluton is 0.705 to 0.706. This reflects the impurity of the fluid within even the most affected limestone samples. The limestone had varying mixtures of its original fluid and that of the pluton; we should not expect the limestone to ever have pure Sage Hen Flat pluton fluid.

Other Factors

We must also note that the Sage Hen Flat pluton alone may not have caused the recrystallization we observed. In the McDoogle pluton of the eastern Sierra Nevada, adjacent plutons radiated heat through newer ones to recrystallize their rock and surrounding layers (Stearns and Bartley, 2015). In the Sage Hen Flat pluton, another unexposed pluton may have further crystallized the surface material. In order to prove if such was the case, we could turn to metamorphic petrology. We could search for certain minerals in the surrounding rock which only form in high temperatures and pressures. We could then examine the size of the pluton and deduce whether or not the pluton was capable of contributing enough heat to form such minerals.

CONCLUSION

In the comparison between the Bilodeau-Nelson (1993) and the Ernst-Hall (1987) interpretations of the contact between the Sage Hen Flat pluton and the surrounding Deep Spring Formation, we analyzed field relations, crystal size changes at varying distances, and changes in isotopic composition of the carbonates. Our data reveal that the physical and chemical changes in the surrounding wall rock and in the pluton likely occurred because of intrusion. The changes we observed in the texture of carbonates and granite near the contact, as well as the evidence of fluid mixing between the carbonates and the granite, strongly suggest that the contact is intrusive and not a simple fault. Our observation of granite dikes also strongly supports this idea. This is in line with the interpretation of the contact proposed by Bilodeau and Nelson (1993).

ACKNOWLEDGEMENTS

The Department of Geological Sciences at the University of North Carolina at Chapel Hill is entirely responsible for providing us with the guidance, equipment, and travel accommodations to complete our research. We would like to acknowledge the Sierra Nevada Aquatic Research Laboratory, as well as the Crooked Creek White Mountain Research Station for lodging accommodations and hospitality. Our research was supported by the Anadarko Petroleum Corporation, the UNC Honors Program, the First-Year Seminar Program, and the Office of Undergraduate Research Graduate Research Consultant Program. We would also like especially credit Prof. Allen Glazner for his oversight of our project, methods, and field work and Prof. Drew Coleman for his individualized guidance in our strontium analysis. We would like to credit Tyler Wickland for helping us obtain our results with his polishing expertise.

REFERENCES CITED

Bilodeau, B. J. and Nelson, C. A., 1993, Geology of the Sage Hen Flat Pluton, White Mountains, California: The Geological Society of America, MGI077, 1:24000.

Coleman, D.S., Briggs, S., Glazner, A.F., and Northrup, C.J., 2003, Timing of plutonism and deformation in the White Mountains of eastern California: Geological Society of America Bulletin, v. 115, p. 48–57, doi: 10.1130/0016-7606(2003)115<0048: TOPADI>2.0.CO;2.

Coleman, D.S., Bartley, J.M., Glazner, A.F., and Law, R.D., 2005, Incremental Assembly and Emplacement of Mesozoic Plutons in the Sierra Nevada and White and Inyo Ranges, California: Geological Society of America Field Forum Field Trip Guide (Rethinking the Assembly and Evolution of Plutons: Field Tests and Perspectives, 7-14 October 2005), p. 42.

Ernst, W.G. and Hall C.A., 1987, Geology of Mount Barcroft-Blanco Mountain area, eastern California: The Geological Society of America, MCH066, 1:24000.

Faure, G., 1986, ed. 2, Principles of Isotope Geology: New York, NY, John Wiley and Sons, Inc., p. 589.

Nelson, C. A., 1966, Geologic map of the Blanco Mountain quadrangle, Inyo and Mono Counties, California: U.S. Geological Survey, GQ-529, 1:62500.

Stearns, M.S. and Bartley, J.M., 2015, Two-stage emplacement of the McDoogle pluton: insights into the early stages of intrusive suite construction, Sierra Nevada, CA.: The Geological Society of America Bulletin. p. 1-7.

Three-dimensional measurement of columnar jointing in the Bishop Tuff, Owens River Gorge, California

Antonio M. Bird, Elizabeth S. Brogden, and Katherine A. Kelker
Department of Geological Sciences, University of North Carolina, Chapel Hill, North Carolina 27599-3315, USA

ABSTRACT

Aerial drone photography, satellite imagery, and scanning electron microscopy were used to form a geologic model of the Bishop Tuff along a 1.5 km segment of Owens River Gorge in eastern California. Columnar joint width is bimodally distributed, with wide, densely-welded joints reaching from the base of the gorge to a section of shorter joints averaging 2-4 meters in width. Elevation and columnar joint width are negatively correlated. Pumice samples taken from fumarolic mounds exhibit secondary mineralization not observed in off-mound samples, explaining their resistance to erosion compared to the surrounding tuff. Fumarolic mounds are not conclusively correlated with the occurrence of nearby columnar jointing.

INTRODUCTION

Columnar jointing occurs in a variety of rocks, but it is most commonly found in basalt flows. Columnar joints form when the rocks cool and contract, breaking and forming into prismatic columns. These columns range in size and often form two or three distinct zones (Spry, 1962). Vertical columns are perpendicular to the cooling surface, but many joints are often curved and sometimes even horizontal (Fig. 1).

The Bishop Tuff is a Pleistocene ignimbrite, covering ~1300 km^2 in eastern California, extending from Mono Lake on the northern end to Bishop on the southern end (Fig. 2). Owens River Gorge runs through the tuff, providing well-exposed cross sections that allow the study of columnar jointing. Whereas columnar jointing has been extensively studied in basalts, such as the nearby Devil's Postpile, the phenomenon is almost undescribed in rhyolite. Our study aimed to gain a greater understanding of rhyolitic columnar jointing, as well as its relationship to fumarolic mounds that surround the gorge.

There is high variation in width and orientation among joints throughout Owens River Gorge. Joints have formed at many different angles. In some areas, joints radiate from a common point, and in other locations, joints are nearly parallel to one another. Whereas the majority of the columnar joints are roughly vertical, some joints lie on a more horizontal axis. The widths of the columnar joints are strongly correlated with their eleva-

Figure 1. Typical "columnar cactus" pattern in Owens River Gorge, with joints radiating from a common point. Columnar joints in the lower zone are wider than the joints in the upper zone.

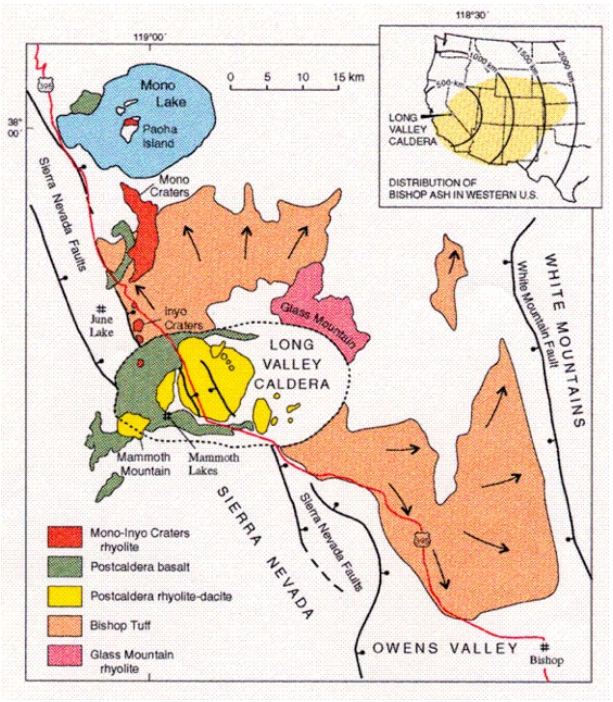

Figure 2. Map of Long Valley Caldera and surrounding areas (USGS, 2016).

tions within the gorge. Toward the top of the gorge, the joints are relatively narrow, whereas near the bottom of the gorge, the columnar joints are significantly wider. These densely-welded joints are known for their world-class climbing routes.

Low fumarolic mounds are prominent throughout the southern part of the Bishop Tuff, typically standing 0.5 meter to 15 meters tall (Sheridan, 1969; Fig. 2). It has been conjectured that the location of radiating columnar joints are related to the location of fumarolic mounds (Putnam, 1960). We hypothesize that radiating columnar joints formed under fumarolic mounds in Owens River Gorge. Furthermore, fumarolic gases are thought to escape through steam conduits within the mounds (Sheridan, 1969). Due to this trend, we hypothesize that gases released have caused secondary mineralization within pumice clasts on fumarolic mounds. Columnar joints could show the lateral path of heat flow escaping the steam conduit (Putnam, 1960).

METHODS

Drone photography

The topography of the gorge was captured in images taken aerially from a DJI Phantom 4 Quadcopter. This drone used a standard 4K camera and an attached near-infrared imagery unit. The drone flew three separate missions to survey the entire area. Each mission covered approximately 0.8 km along the gorge. Geolocation was recorded by an onboard GPS and photos from each camera were taken every 2-3 seconds during preprogrammed flights located 300 feet above ground level. Over a thousand photos from a variety of angles were taken of the gorge and the area surrounding it.

Modeling and image analysis

Models of Owens River Gorge and its columnar jointing were created using computer software. Three-dimensional models and digital elevation maps were processed using DroneDeploy, a cloud-based mapping application. Orthophotos were processed with Agisoft PhotoScan software. A three-dimensional model of the entire gorge was created alongside individual models of each of the three missions flown.

Figure 3. Image of fumarolic mounds throughout Bishop Tuff, California. Photo by Allen Glazner.

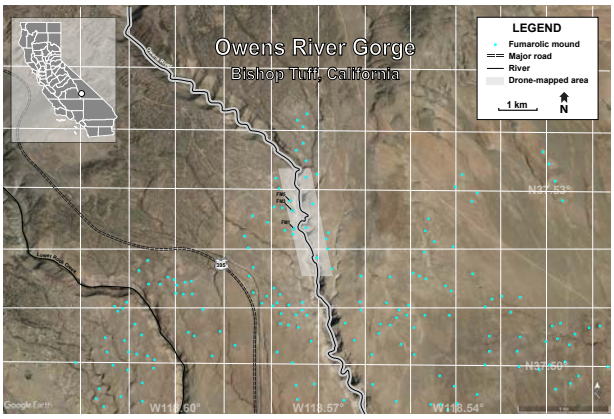

Figure 4. Map of Owens River Gorge, Bishop Tuff, California, including locations of fumarolic mounds and area surveyed by drone.

Widths of columnar joints at different elevations within the gorge were measured using the DroneDeploy distance measuring tool. Elevations were determined from the 3D model. We measured 137 joints. Within each area of columnar jointing, all discernable joints were measured in order to capture a large sample size of joint widths. Joints were measured at a variety of locations within the gorge, so the sample measurements are representative of jointing throughout the entire gorge.

Furthermore, the three-dimensional model in DroneDeploy was utilized to observe the relationship between the locations of fumarolic mounds and radiating columnar joints. All mounds and joint areas were flagged and their locations were recorded. This allowed the locations of the mounds and joints to be easily compared to one another, so any correlation between the two could be seen.

Electron microscopy

Five fumarolic mounds on the west side of the gorge were identified for sampling. For each mound selected, two samples were retrieved: one from the highest point on the mound and one 25 to 50 meters away from the mound. In preparation for analysis under a microscope, some samples were cut into small pieces, carbon-coated, and mounted on to stubs. Later samples were coated in epoxy and polished in rounds. Pumice composition and secondary mineralization were evaluated for each sample, using one of two scanning electron microscopes: a Tescan VEGA 5136, in the Geological Sciences department, or a Hitachi S-4700, in the Chapel Hill Analytical Nanofabrication Laboratory (CHANL).

RESULTS

Within the layer directly below the rim of the gorge, the joints range between 2 and 4 meters in width, and have an average height of around 20 meters. The layer near the bottom of the gorge contains joints ranging between 10 and 25 meters in width. These wide columns average around 50 meters tall. In between these two zones is a small layer with minimal columnar jointing. This layer of the Owens River Gorge wall only accounts for a small percentage of the surface area of wall, but it is effective in showing the division between the two zones of the columnar joints. These relationships resemble those in Staffa, Scotland where columnar jointing in basalts toccurs in either two or three separate zones (Phillips, 2013). Based on the data collected, it is not clear whether Owens River Gorge relates more to the zoning exhibited in part a or b of Figure 5. Columnar jointing in Owens River Gorge could be a modification of the more common three-zone model of columnar jointing, with a small entablature, or it could reflect the less common model with only two distinct zones.

The upper layer appears to correspond with the Ig-2Eb zone of Wilson and Hildreth (2003), whereas the lower layer is the earlier-deposited Ig1Eb ignimbrite unit. Ig2Eb is 30-70% rhyolite in its lithic component, whereas Ig1Eb is lithic poor (Wilson and Hildreth, 2003).

Figure 6 illustrates the relationship between elevation and width of columnar joints in the north, middle, and south regions of the gorge. In the gorge, as elevation decreases from the rim, there is a sharp jump from closely spaced joints to widely spaced joints. The elevation of this transition descends from north to south.

The data above appear skewed by sampling bias, because a greater quantity of joints was measured at higher elevations within the gorge than at lower elevations. When the log of the widths of the columnar joints is taken, the data form two approximately standard normal curves: one curve for the joints forming at higher elevations and another curve for the wider joints that are closer to the bottom of the gorge (Fig. 7). The mean of the smaller joints is 1.33 m and the mean of the larger joints is 13.57 m.

Contrary to Putnam's observations, there is no obvious relationship between radiating columnar joints and fumarolic mounds. While there are many instances in which fumarolic mounds on the edge of the gorge have radiating columnar jointing directly underneath, there are also multiple areas of radiating columnar jointing that are not near any fumarolic mound. Also, this theory does not account for the few cases in which there is a fumarolic mound on the edge of the gorge, but no radiating columnar jointing present underneath the mound.

Pumice samples gathered from fumarolic mounds show evidence of secondary mineralization under a scanning electron microscope. Samples from fumarolic mounds show pervasive development of spherical structures approximately 200 mm in diameter (Fig. 8). These structures were not found in samples gathered away from the fumarolic mounds. The shells of the spheres are pure SiO_2 and are likely either tridymite or cristobalite, common vapor-phase minerals in ignimbrites. The interior of the spheres appears to be altered volcanic glass. The secondary mineralization present in the pumice clasts is likely a result of hot gases that once flowed through the fumarolic mounds in the years or decades following the eruption.

DISCUSSION

The presence of secondary mineralization may explain why many fumarolic mounds have not been eroded away on the edge of the gorge and in between river meanders. The secondary minerals tridymite and christobalite cause cementation of the soft, fragile volcanic ash (Cas and Wright, 1988). In many places along the rim of Owens River Gorge, the edge of a fumarolic

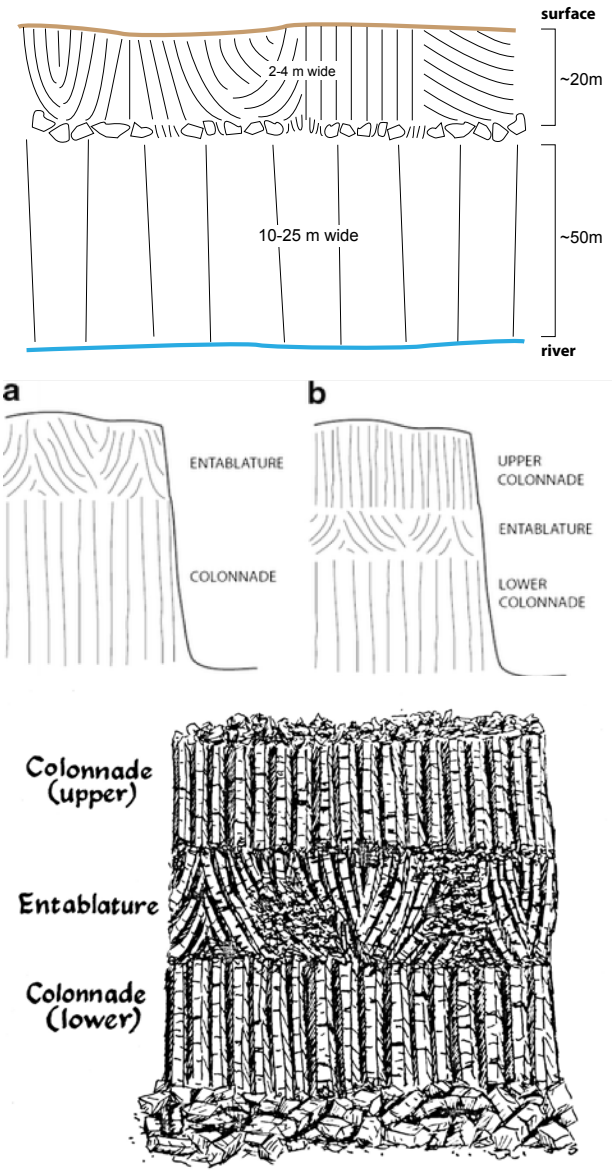

Figure 5. Typical zonation of columnar jointing within the tuff compared to possible zonation of columnar jointing (Phillips, Williams).

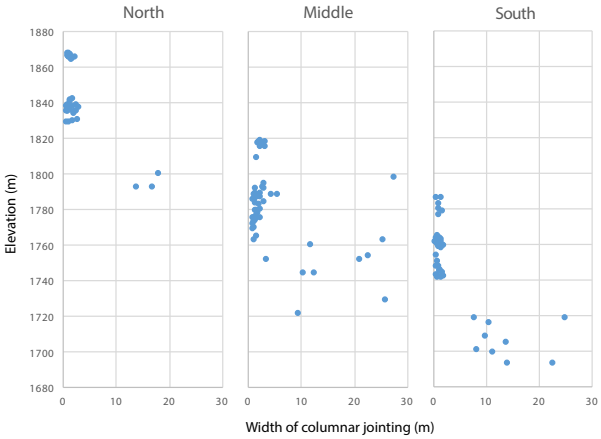

Figure 6. Column width by elevation in the north, middle, and south areas of the gorge.

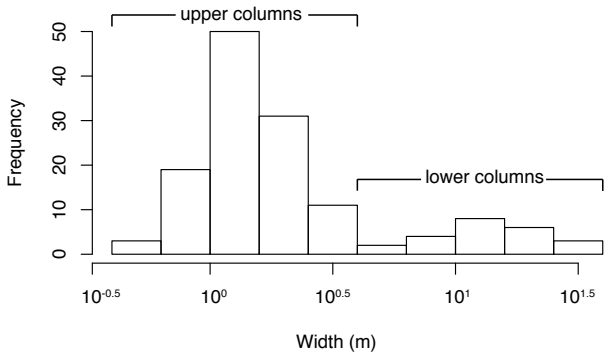

Figure 7. Frequency of columnar joints by width, forming two normal distributions (corresponding to upper and lower elevation) on a log scale.

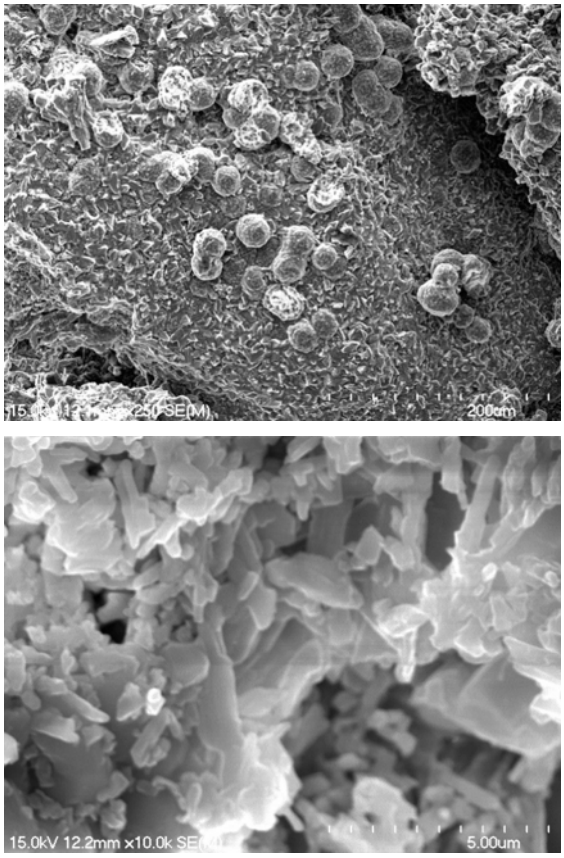

Figure 8. Pumice sample from a fumarolic mound with evidence of secondary mineralization (top). Off-mound pumice sample (bottom).

mound is slightly visible above an area of radiating columnar joints. In these places, an entire mound was likely present at some point in the past, but erosional widening of the gorge has removed most of it. In other areas along the gorge's rim, there are abundant radiating columnar joints, but no obvious fumarolic mounds. However, a ridge is visible a short distance from the rim of the gorge. This ridge has orange-tinted soil on top of it, and white-tinted soil lies between it and the gorge. White-tinted soil occurs on the tops of many fumarolic mounds in other areas of the gorge. If white-tinted soil is indicative of the presence of a fumarolic mound, then perhaps fumarolic mounds once existed in the space that lies between the ridge and the rim of the gorge. These mounds could have been eroded off the surface of the gorge. If this is the case, then all of the radiating columnar jointing on the walls of Owens River Gorge may have resulted from the presence of fumarolic mounds. To test this theory, one could look for secondary mineralization in samples gathered from the area between the ridge and the gorge rim.

CONCLUSION

A consistent zonation of columnar jointing was observed along the wall of Owens River Gorge. It is clear from the columnar cactus pattern (Fig. 1) and aerial imagery that joint width is correlated with elevation, and sharply changes at different elevations below the rim. The hypothesis that radiating columnar jointing outcrops are only present under fumarolic mounds was not supported. There were many instances of overlap between the locations of radiating columnar joints and fumarolic mounds; however, many radiating columnar joints could not be linked to a nearby fumarolic mound. Finally, the hypothesis that secondary mineralization has formed in the pumice clasts on fumarolic mounds is sustained. The samples collected from on top of the fumarolic mounds contained spherical SiO_2 structures not present in samples taken away from the mound, creating a more coherent, erosion resistant rock.

ACKNOWLEDGMENTS

We would like to thank the Department of Geological Sciences at the University of North Carolina at Chapel Hill, the Anadarko Petroleum Corporation, the UNC Honors Program, the First-Year Seminar Program, the Office of Undergraduate Research Graduate Research Consultant Program, the staffs of the Sierra Nevada Aquatic Research Laboratory and Crooked Creek Station of the White Mountain Research Center, Jeff Glazner of Salix Consulting, Inc., Tyler Wickland, John Boyd, Emma Blackwell, Megan Raisle, Dr. Drew Coleman, and Dr. Allen Glazner.

REFERENCES CITED

Cas, R.A.F., and Wright, J.V., 1988, Volcanic Successions- Modern and Ancient: Chapman and Hall, p. 258.

Phillip, J.C., Humphreys, M.C.S., Daniels, K.A., Brown, R.J., and Witham, F., 2013, The formation of columnar joints produced by cooling in basalt at Staffa, Scotland: Bulletin of Volcanology, v.75, p. 1-17.

Putnam, W.C., 1960, Origin of Rock Creek and Owens River Gorges, Mono County, California: Univ. of California Publications in Geological Sciences, v. 34, p. 221-280.

Sheridan, Michael F., 1969, Fumarolic mounds and ridges of the Bishop Tuff, California: Geological Society of America Bulletin, v. 81, p. 851-868.

Spry, Alan., 1962, The origin of columnar jointing, particularly in basalt flows: Journal of the Geological Society of Australia, v. 8, p. 191-216.

USGS, 2016, Geologic history of the Long Valley, Mono Basin region: https://volcanoes.usgs.gov/volcanoes/long_valley/geo_hist_summary.html (accessed December 2016).

Williams H, McBirney AR. 1979. Volcanology. San Francisco (CA): Freeman, Cooper.

Wilson C.J.N., and Hildreth W. 2003, Assembling an ignimbrite: mechanical and thermal building blocks in the Bishop Tuff, California: Journal of Geology, v. 111, p. 653-670.

Strontium isotopic variations in natural waters in eastern California

Austin Kisner, Kelly Cuthbertson, Emily Kian
Department of Geological Sciences, University of North Carolina, Chapel Hill, North Carolina 27599-3315, USA

ABSTRACT

Seventeen natural water sources in eastern California were sampled and analyzed using thermal ionization mass spectrometry and ICP-MS in order to determine $^{87}Sr/^{86}Sr$ and elemental concentrations. Differences in these ratios and concentrations across sampling locations reveal the intrusion of groundwater from hot springs that has interacted with older rock than that of the surface water. Springs that have interacted with Precambrian and Mesozoic rocks have high $^{87}Sr/^{86}Sr$. The springs release water with high $^{87}Sr/^{86}Sr$ and Sr concentrations into Owens River and Hot Creek, causing the areas of Owens River and Hot Creek downstream from the springs to have higher $^{87}Sr/^{86}Sr$ than those upstream.

INTRODUCTION

Strontium is frequently used as a geochemical tracer to gain insight into subsurface water rock interactions. Strontium tracing techniques were applied to study a variety of bedrock sources in eastern California (Fig. 1). For rocks containing Sr and Rb, the number of ^{84}Sr, ^{86}Sr, and ^{88}Sr atoms in the rock will remain constant, whereas the number of ^{87}Sr atoms in rocks increases as a result of β-decay of ^{87}Rb. This relationship between the atomic ratios of $^{87}Sr/^{86}Sr$ and Rb/Sr is modeled by the equation below, where lambda is the decay constant and t is age of the rock:

$$(^{87}Sr/^{86}Sr)_{now} = (^{87}Sr/^{86}Sr)_{initial} + (^{87}Rb/^{86}Sr)_{now}(e^{\lambda t}-1)$$

As seen in this equation, the initial strontium ratio and age of the rock factor into the $^{87}Sr/^{86}Sr$ ratios of present-day sources. Hence, the geochemical origin and the relative age of rocks can be determined through the use of Sr isotopes. A high ratio of $^{87}Sr/^{86}Sr$ often reflects groundwater that has been exposed to older rocks, whereas a lower ratio of $^{87}Sr/^{86}Sr$ often reflects groundwater that has been exposed to younger rocks as there has been less time for ^{87}Rb in the rocks to decay to ^{87}Sr. Two rocks that are of similar age yet contain significantly different $^{87}Sr/^{86}Sr$ must have differing geochemical compositions (Shand et al., 2009) For these reasons, an extensive amount of research involving the use of Sr isotope ratios as natural tracers of bedrock age and composition has been done (Capo et al. 1998; Gosselin et al., 2004; McNutt, 2000; Bullen et al., 1996).

ICP-MS and thermal ionization mass spectrometry (TIMS) were performed on a variety of natural spring, river, lake, and creek water samples from eastern California with the goal of determining each sample's $^{87}Sr/^{86}Sr$ ratios and elemental concentrations. These Sr ratios and elemental concentrations can be used to investigate the impact of spring water intrusion on river water ratios and concentrations, shifts in Sr concentration at previously sampled sites, and the relationship between bedrock characteristics and $^{87}Sr/^{86}Sr$. In this area, the age of the rocks range from Proterozoic to Quaternary. Three previously sampled sites were resampled (Owens River, Mono Lake, Whitmore Tubs) as part of an ongoing study done by 72H students.

METHODS

Seventeen water samples were collected and filtered with a 45 μm filter into 15 mL Savillex beakers. Samples were

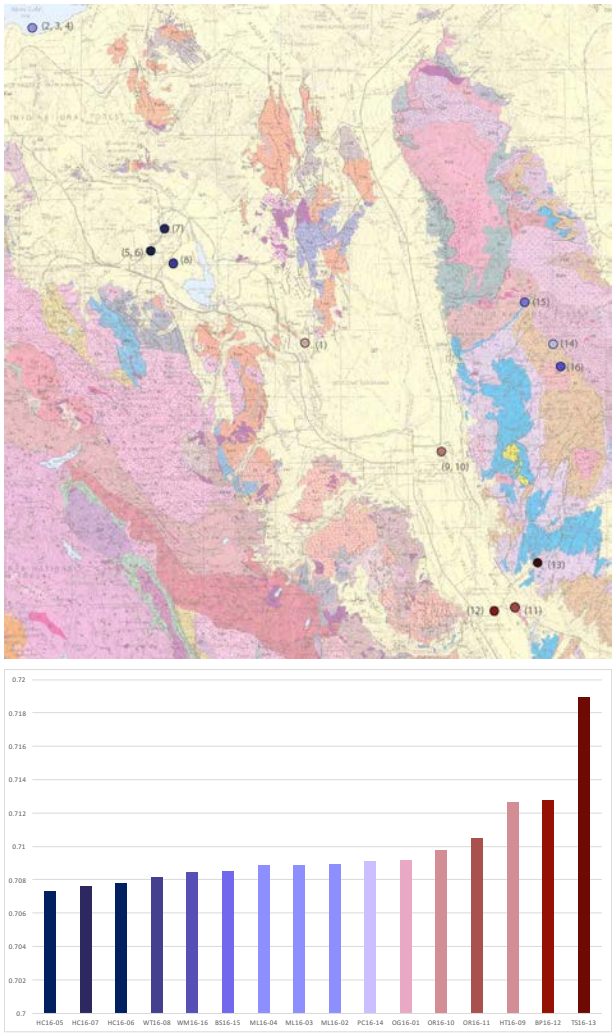

Figure 1: Geologic map of sampling locations in Eastern California with a graph of $^{87}Sr/^{86}Sr$ ratios in corresponding colors.

spiked with ^{84}Sr tracer, dried, and then redissolved in 525 μL 3.5M HNO_3. Strontium was isolated using Sr-spec™ resin following standard UNC Geological Sciences protocol. One drop 0.25 M H_3PO_4 was added and samples were evaporated to dryness before being loaded onto single Re filaments. Two μL TaF_5 was added and the samples were evaporated to dryness. Samples were loaded into the VG-Sector-64 thermal ionization mass spectrometer housed in the Geological Sciences Department at UNC. Samples were analyzed in triple-dynamic mode with ^{88}Sr = 3V using 10^{11} ohm resistors. Samples were corrected for mass fractionation assuming $^{86}Sr/^{88}Sr = 0.11940$ and exponential fractionation behavior. Replicate analyses of NBS-987 yield $^{87}Sr/^{88}Sr$ = 0.710269 +/- 0.000015 (2σ). For ICP-MS analysis, samples were acidified by adding concentrated HNO_3 in a ratio of 2:100. Samples were analyzed by inductively coupled plasma mass spectrometry using the

Agilent ICP-MS housed in the Geological Sciences Department at UNC. The ICP-MS was calibrated using the standard solutions of normal concentrations for each element. Peaks monitored were ^{39}K, ^{43}Ca, ^{44}Ca, ^{47}Ti, ^{85}Rb, ^{88}Sr, ^{89}Y, and ^{238}U.

RESULTS

Variation in $^{87}Sr/^{86}Sr$ ratio and Sr concentration of samples taken in Owens River and Hot Creek show the impact of groundwater on the geochemical composition of the rivers (Fig. 2). Water samples tested upstream from natural springs in Hot Creek show $^{87}Sr/^{86}Sr$ ratios and Sr concentrations that are lower than samples taken from the spring. Owens River exhibited this pattern as well with upstream samples having lower $^{87}Sr/^{86}Sr$ ratios and Sr concentrations than samples taken from the spring. Downstream $^{87}Sr/^{86}Sr$ ratios and Sr concentrations in Hot Creek and Owens River are higher and fall roughly between that of the upstream and spring samples.

Upstream water samples from Hot Creek exhibited a higher Ca concentration than the spring samples and downstream samples. Upstream water samples from Owens River exhibited a lower Ca concentration than the spring samples and downstream samples (Table 1).

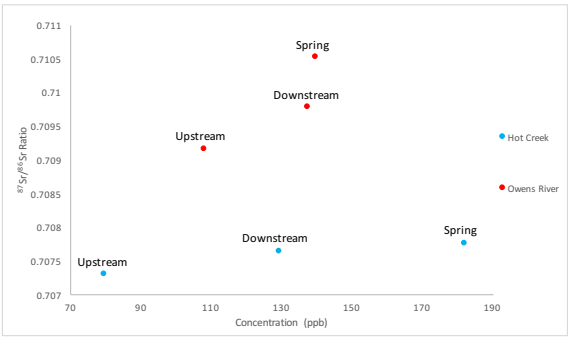

Figure 2: Calcium concentration vs. $^{87}Sr/^{86}Sr$ ratio in Hot Creek and Owens River.

DISCUSSION

Impact of Springs On River

Upstream samples from Hot Creek and the Owens River (Fig. 2) consist primarily of precipitation that has collected in the rivers; therefore the $^{87}Sr/^{86}Sr$ and Sr concentrations of these samples are low and do not reflect interactions with old rocks. However, other samples from these areas (HC16-06 and OR16-11) were directly sampled from spring sources. The $^{87}Sr/^{86}Sr$ and Sr concentrations of these samples are higher than that of upstream samples (Fig. 2) due to the subsurface interactions of spring water and older bedrock. The $^{87}Sr/^{86}Sr$ in samples collected downstream (OR16-10 and HC16-07) reflect these increased ratios and concentrations as the $^{87}Sr/^{86}Sr$ and Sr concentrations fall between the values recorded for upstream and spring samples. This trend shows the effect of natural springs on Owens River and Hot Creek surface waters. Water released into the rivers at the source of the springs is high in both $^{87}Sr/^{86}Sr$ and Sr concentration. The high ratios and concentrations of the springs are then diluted as the upstream waters mix with the spring water, resulting in $^{87}Sr/^{86}Sr$ and Sr concentrations downstream of the spring that are slightly higher than those of upstream waters.

Elemental Concentrations

ICP-MS analysis allows for comparison of various common cations, including K, Ca, Ca, Ti, Rb, Sr, Y, and U across spring locations. The bedrock over which the water flows can contribute to the concentration of ions, as in the case of Ca. Several of the springs sampled flow over carbonate rocks such as limestone ($CaCO_3$). Precambrian carbonate rocks tend to have a higher $^{87}Sr/^{86}Sr$ ratio and Ca concentration but lower K and Rb concentrations than the Mesozoic granites common to the area (Fig. 3). These granites tend to have lower $^{87}Sr/^{86}Sr$ ratios and Ca concentrations but higher K and Rb concentrations (Fig. 3). The alluvium found between the Sierra Nevada Range and White Mountains is a mixture of Proterozoic and Mesozoic rocks, making it difficult to distinguish the age of the bedrock from where the water samples were sourced (D. Coleman, personal communication, 2016). The Toll House spring sample, located above Proterozoic carbonates, showed higher $^{87}Sr/^{86}Sr$ ratios and Ca concentration with lower K and Rb concentrations. The Crooked Creek, Poison Creek, and Barcroft Station samples were all located above Mesozoic granitic rock and showed lower $^{87}Sr/^{86}Sr$ ratios and Ca concentration with higher K and Rb concentrations. Water samples from the caldera, sourced from Cenozoic volcanic rocks, also showed lower $^{87}Sr/^{86}Sr$ ratios and Ca concentration with higher K and Rb concentrations (Fig. 3).These variations are consistent with the varying geochemical composition of the rocks. Comparison of the $^{87}Sr/^{86}Sr$ ratios to known bedrock compositions of sampled locations supports the positive correlation between higher $^{87}Sr/^{86}Sr$ ratios and water-rock interactions involving older rocks.

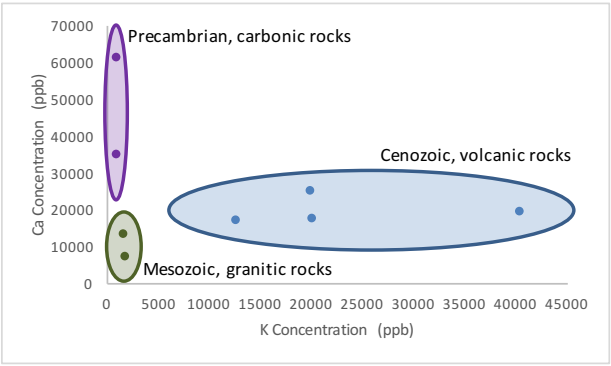

Figure 3: K Concentration vs. Ca concentration in various rock types.

Age of Bedrock and $^{87}Sr/^{86}Sr$

Multiple maps of bedrock in eastern California were used to estimate the relative age of the bedrock of waters sampled. As predicted, waters interacting with young rocks of the Quaternary and Tertiary periods have low $^{87}Sr/^{86}Sr$, whereas the waters interacting with old rocks of Proterozoic age have high $^{87}Sr/^{86}Sr$. However, waters sampled from areas with Mesozoic bedrock had unusually low $^{87}Sr/^{86}Sr$ (Fig. 4). It is possible that these sampling sites contained rocks that originally came from other sources and were not of the Mesozoic period. Another possible explanation for these low $^{87}Sr/^{86}Sr$ ratios is that the original geochemical composition of the bedrock was low in $^{87}Sr/^{86}Sr$.

Continuation of 72H Study

Data collected from previous 72H studies in 2012 and 2015 were used to determine whether $^{87}Sr/^{86}Sr$ ratios and Sr concentrations of waters sampled in Whitmore Tubs, Mono Lake, and Owens River have changed over time. The $^{7}Sr/^{86}Sr$ ratios and Sr concentrations in all three locations over the years have been fairly consistent, and they fall within the ranges of error (Fig. 5).. Changes in water levels, variations in water flow paths, and discrepancies in sampling locations are all possible causes for changes in $^{87}Sr/^{86}Sr$ ratios and Sr concentrations.

Table 1: ICP-MS elemental concentrations and TIMS $^{87}Sr/^{86}Sr$

Sample Location	39 K [No Gas]	43 Ca [No Gas]	44 Ca [No Gas]	47 Ti [No Gas]	85 Rb [No Gas]	88 Sr [No Gas]	89 Y [No Gas]	89 Y [He]	238 U [No Gas]	87Sr/86Sr
OG16-01	7588.696385	20426.61515	19992.1668	0.860379647	19.99336849	108.0534909	0.004446977	0.005290956	3.850750231	0.709162
ML16-02	20001.07586	24639.85448	24439.44154	5.071141293	4.000787116	230.4374857	0.002067191	0.001824342	20.33144458	0.708917
ML16-03	40478.06398	18883.25547	18856.94043	7.547421337	44.46670907	298.1005361	0.003341197	0.004561037	26.15030292	0.708864
ML16-04	OR	2312.416628	2263.100267	31.39765586	285.5123598	14.81809989	0.440794374	1.268599251	36.08265116	0.708867
HC16-05	5345.197297	19195.96085	19238.0307	3.668609358	9.375083647	79.78567627	0.008714132	0.026271798	2.060190517	0.707306
HC16-06	12641.20291	16594.4529	16202.12674	3.632818181	84.23837652	181.9950454	0.009675687	0.029920664	1.158558755	0.707756
HC16-07	9057.725775	17956.37173	17623.59561	2.681194985	47.81094425	129.4289075	0.009807871	0.027184334	1.804115733	0.707645
WT16-08	20218.93465	17217.97508	16854.60461	4.762109473	140.7044847	250.1333339	0.007884629	0.033569712	0.349874609	0.708162
HT16-09	8376.634769	40591.83247	39721.43643	3.457423374	4.699916211	370.4789961	0.004326799	0.020068854	6.361241155	0.71266
OR16-10	6002.422624	26529.62303	25720.23399	1.200661249	14.06985207	137.3578529	0.0118274	0.056923475	5.97142638	0.70978
OR16-11	5234.623434	26114.41419	25394.10725	1.222927888	11.39830738	139.7600471	0.023489194	0.100348464	5.340843042	0.710518
BP16-12	3931.019758	30605.66921	29172.64337	11.49130572	1.781942967	1144.506398	0.012861302	0.100896678	1.132173054	0.712768
TS16-13	961.3117588	60704.94023	58955.17328	0.887123992	0.442339456	781.3840505	0.00270423	0.049078258	3.584006041	0.718927
PC16-14	1061.438229	34656.51961	33863.98477	0.797163967	0.622056029	57.55421658	0.006814829	0.033022592	0.886386016	0.709112
BS16-15	1803.192632	7010.360089	6522.161429	0.637490802	0.61421816	78.95690844	0.003016692	0.020251653	0.072854014	0.708502
WT16-16	1784.278131	12930.86594	12493.8333	0.817379162	1.783326447	150.8536126	0.001442218	0.01587232	0.924373264	0.708435
PW16-17	OR	370573.8023	357748.6826	4.223637108	493.749106	9552.568391	0.027962214	1.189312083	0.392825445	0.712767

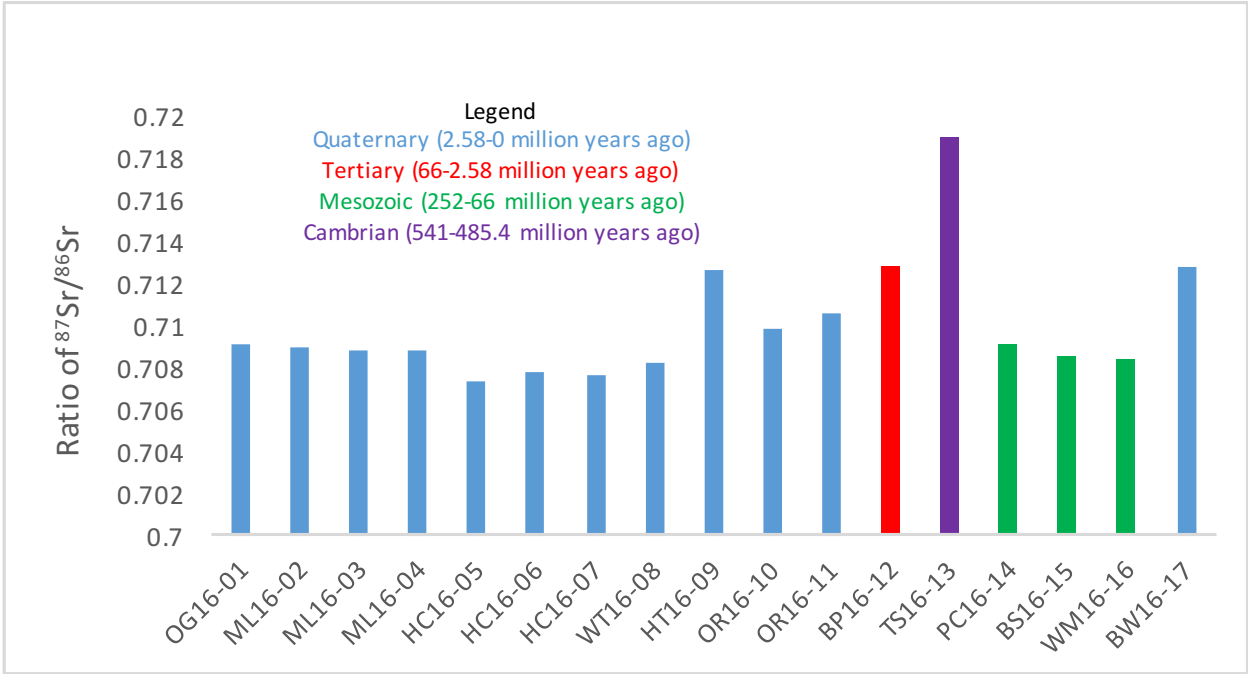

Figure 4: $^{87}Sr/^{86}Sr$ ratio of of waters distinguished by variously aged bedrock.

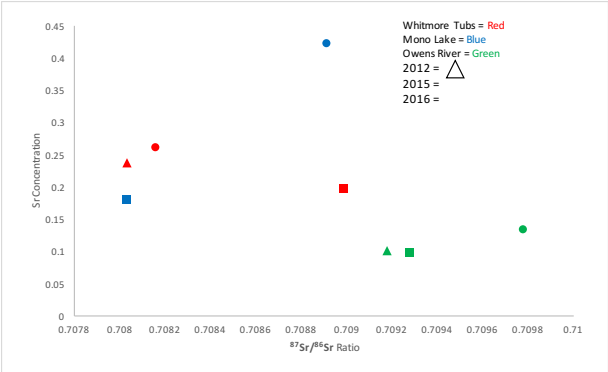

Figure 5: Time Comparison of $^{87}Sr/^{86}Sr$ ratio and Sr Concentration

Limitations and Improvements

Sampling from more of the locations that had been studied by 72H students in the past would have allowed a better analysis of trends in $^{87}Sr/^{86}Sr$ ratios over time. Future 72H students should continue to study $^{87}Sr/^{86}Sr$ ratios of natural waters in eastern California to track changes in these water sources over time. Future research on this subject should include collection of rock samples from each water source to more accurately analyze relationships between $^{87}Sr/^{86}Sr$ ratios and age of bedrock.

CONCLUSIONS

Isotopic analyses of water samples from eastern California show that natural springs introduce water with high $^{87}Sr/^{86}Sr$ into the surface water of Owens River and Hot Creek, causing the geochemical composition of downstream waters to be higher $^{87}Sr/^{86}Sr$ than that of upstream waters. ICP-MS analysis shows that older rocks have higher Sr ratios and Ca concentrations but lower Rb and K concentrations. The $^{87}Sr/^{86}Sr$ ratios of these waters reveal a trend that water interacting with older rocks results in higher $^{87}Sr/^{86}Sr$ ratios than water interacting with younger rock, except waters sampled from Mesozoic bedrock. Low $^{87}Sr/^{86}Sr$ ratios of Mesozoic samples could be due to (1) the intrusion of newer rocks within sampled areas or (2) low $^{87}Sr/^{86}Sr$ in initial geochemical composition of the bedrock. The $^{87}Sr/^{86}Sr$ in Owens River and Crooked Creek increased since 2012 and 2015 respectively, whereas the $^{87}Sr/^{86}Sr$ in Mono Lake decreased since 2015. Continued sampling of these spring sites over time will improve long term trends for $^{87}Sr/^{86}Sr$ and Sr concentrations.

ACKNOWLEDGMENTS

This research was supported by the Department of Geological Sciences at the University of North Carolina at Chapel Hill, the Anadarko Petroleum Corporation, the staffs of the Sierra Nevada Aquatic Research Laboratory and the Crooked Creek Station of the White Mountain Research Center, the UNC Honors Program, the First-Year Seminar Program, and the Office of Undergraduate Research Graduate Research

Consultant Program. We would like to specially thank Ashley Cocciadiferro, Sean Gaynor, and Dr. Xiao-ming Liu for their invaluable guidance and assistance during our time working in the Isotope Geochemistry Lab. We would also like to thank Emma Blackwell, Tyler Wickland, and John Boyd for their greatly-appreciated assistance in the field. We are grateful to the entire 72H team of students for making this trip a truly unforgettable experience. Lastly, we would like to express our deepest gratitude to Dr. Allen Glazner and Dr. Drew Coleman for creating such an incredible seminar, organizing the trip of a lifetime, and providing us with the wisdom, encouragement, and guidance needed for us to successfully to conduct this study and develop great research skills.

REFERENCES CITED

Batemen, P., 1992, Plutonism in the central part of the Sierra Nevada batholith, California: U.S. Geological Survey Map - 1483, scale 1:250,000.

Bullen, T.D., Krabbenhoft, D.P., and Kendall, C., 1996, Kinetic and mineralogic controls on the evolution of groundwater chemistry and $8^{7}Sr/^{86}Sr$ in a sandy silicate aquifer, northern Wisconsin, USA: Geochimica et Cosmochimica Acta, v. 60, p. 1807–1821.

.Capo, R.C., Stewart, B.W., and Chadwick, O.A., 1998, Strontium isotopes as tracers of ecosystem processes: theory and methods: Geoderma, v. 82, p. 197–225.

Geologic Map of California, http://maps.conservation.ca.gov/cgs/gmc (accessed December 2016).

Gosselin, D.C., Harvey, F.E., Frost, C., Stotler, R., and Macfarlane, P.A., 2004, Strontium isotope geochemistry of groundwater in the central part of the Dakota (Great Plains) aquifer, USA: Applied Geochemistry, v. 19, p. 359–377.

McNutt, R.H., 2000, Strontium Isotopes: Environmental Tracers in Subsurface Hydrology, Springer US, p. 233–260.

Shand, P., Darbyshire, D., Love, A., and Edmunds, W., 2009, Sr isotopes in natural waters: Applications to source characterisation and water–rock interaction in contrasting landscapes: Applied Geochemistry, v. 24, p. 574–586.

Lead concentrations in pine trees in eastern California: variations with time period and distance from Highway 395

Lindsay Barnes, Sarah Brooker, Molly Paul, and Julia Tian
Department of Geological Sciences, University of North Carolina, Chapel Hill, North Carolina 27599-3315, USA

ABSTRACT

Lead is a toxic metal used in the 1950's without full knowledge of the environmental consequences. With the goal of studying variations in environmental Pb concentrations over time and distance from Highway 395, a major highway in eastern California, four trees were analyzed by taking tree cores, separating Pb from decadal intervals, and determining Pb concentrations and isotope ratios with a thermal ionization mass spectrometer. In trees A and B, $^{206}Pb/^{207}Pb$ drops from older (1976-1985) to younger (1996-2005) samples. This is consistent with uptake of anthropogenic Pb with $^{206}Pb/^{207}Pb$ lower than ambient environmental Pb. Published analyses of Pb in leaded gasoline from southern California gas stations have the required low $^{206}Pb/^{207}Pb$ ratios. The concentration of the Pb indicates that trees closer to the highway showed a steady decrease in Pb after regulatory legislation was passed. Our data suggest that anthropogenic Pb from leaded gasoline is slowly being phased out of the biosphere because its isotopic signature is visible in even the recent samples of tree rings.

INTRODUCTION

Lead (Pb) originates from two main sources - natural and anthropogenic. Trees rings serve as a living timeline documenting the concentrations of Pb along with other elements. These rings occur due to annual cycles of growing seasons and serve as a point of reference for our study of Pb isotope ratios and Pb concentration in tree rings over time (Phipps and McGowan, 1993).

California was one of the first states to take action in lowering Pb concentrations in leaded fuel and other products such as paint. It was one of the first states to pass a right -to-know law, which required manufacturers to give notice to the consumers when they were exposed to toxic chemicals (Oudijk, 2010). This paper conducts Pb concentration analysis within trees alive during the time of changing Pb regulation policy. By isolating significant decades when Pb legislation occured, the accumulation and persistence of Pb could be measured over these formative time intervals for environmental regulation.

Lead concentrations in trees are indicative of the environment the tree was living in during the years it was growing (Komarek et al., 2008). Two groups of two trees (Fig. 1) each were selected for study. The first pair of trees was sampled within 200 meters of Highway 395, a major highway that runs approximately north-south in eastern California. These trees were growing when Pb was introduced to gasoline in 1959 and would have experienced significant atmospheric Pb deposition (Sawyer, 1993). The second group of trees was located around 16 kilometers away from the nearest paved road. These trees would also have been growing in the year 1959, but they would not have been directly exposed to high quantities of atmospheric Pb from automobile exhaust. We expect Pb levels to be greater in trees closer to Highway 395 than those further away from the highway and the concentration of Pb in the trees to decrease once leaded gasoline regulation was introduced.

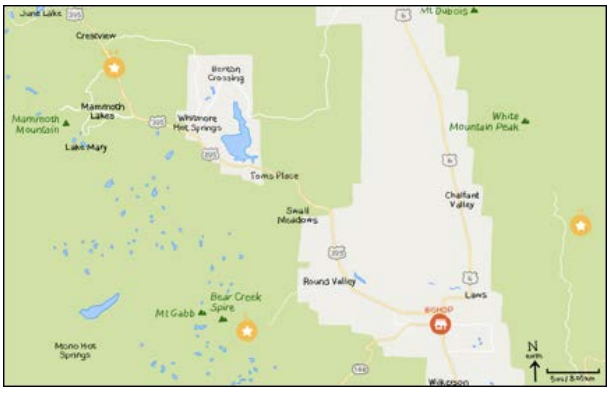

Figure 1. Map of the tree locations used for sampling. The top left is where Trees A & B were sampled. The bottom left is Tree E, and the one to the far right is Tree H.

METHODS

Data Collection

Both trees near Highway 395 were Jeffrey pines (*Pinus Jeffreyi*) in the vicinity of Mammoth Lakes. Tree E was a lodgepole pine (*Pinus contorta*) in the Pine Creek area. Tree H was a limber pine (*Pinus flexilis*) near Crooked Creek Station in the White Mountains. Healthy, century-old pine trees were identified and then sampled using an increment borer. The age estimate of the tree was based on knowledge of the average diameter of the same species of a similar age. Upon identification of a viable tree, the coordinates were recorded using a GPS. The trees were sampled according to the methods described inAgee and Huff (1986). The samples were placed in a plastic bag with the bark side down. The bark shavings were poured into the bottom of the bag. The bag was rolled and taped to prevent the core from moving. The tree cores were sliced into 10-year intervals and labeled as shown in Table 1.

Table 1. Decades analyzed and the corresponding tree. The decades were chosen based on information about the introduction of leaded gasoline (Needleman, 1999).

	Bark	1996-2005	1976-1885	1956-1965	Before 1945
Tree A	A1	A3	A5	A7	A9
Tree B	B1	B3	B5	B7	B9
Tree E	E1	E3	E5	E7	E9
Tree H	H1	H3	H5	H7	H9

Data Analysis

The tree rings were photographed and counted. Four trees were selected for analysis (A, B, E, and H). Five samples for the decades of interest (shown in Table 1) in each tree were ashed in a crucible, increasing the temperature 50 ºC every 30 minutes until the final temperature reached 600 ºC over the course of eight hours. The ash was weighed in 7N HNO_3 in a 7 mL Savillex beaker. The acid solutions were spiked with ^{205}Pb, in 1.1N HBr, and the mass of spike was recorded. The samples were then dried on a hot plate.

Lead was isolated using anion exchange column chromatography (following standard UNC protocol) with 1.1N HBr and 6N HCl. The samples were loaded onto single Re

Figure 2. Left: Jeffrey pine tree adjacent to Highway 395 near Mammoth Lakes. Middle: Lodgepole pine in Pine Creek, far from Highway 395. Right: Limber pine in White Mountains, far from Highway 395.

filaments using H_3PO_4 and silica gel and were then evaporated to dryness. The samples were then loaded into the Phoenix-X-62 thermal ionization mass spectrometer housed in the Geological Sciences Department at the University of North Carolina at Chapel Hill. The samples were analyzed in static multicollector mode with ^{208}Pb = 500 mV using 10^{11} Ω resistors. Samples were corrected for mass fractionation assuming 0.12% amu and linear fractionation behavior.

RESULTS

Tree ring $^{206}Pb/^{207}Pb$ ratios range from 1.210 to1.184. Sample E3 was an outlier with a value of 1.385 and is not shown in the following figures. The ratios and concentrations of Pb in bark are not directly comparable to the ratios in the rings themselves, so trends over time can only be ascertained from looking at the tree rings. The expected Pb isotope signature of leaded gasoline in California is between 1.115 and 1.160 shown in Fig. 5.

DISCUSSION

In Figure 4 the data reveal that the Pb concentrations for the trees farther from the road (Trees E and H) are lower than those closer to the road (Trees A and B) in the years ranging from 1956-1965, when leaded gasoline was introduced. During the years of 1976-1985 and 1996-2005, the Pb concentration does not vary as much among the location of the trees. This shows that as leaded gasoline was phased out, the Pb concentrations evened out since anthropogenic sources of Pb in the environment were declining during those times. Also shown in Fig. 4, there is a trend of decreasing Pb concentration over time. Overall, the amount of Pb found in both the trees close and far from the highway decreased as the consumption of leaded gasoline declined.

In Figure 3, the data shifts toward the signature ratios of leaded gasoline during the time period when leaded gasoline was widespread. The dip in the data toward the ratio signature of leaded gasoline indicates this trend. This dip begins to appear in the years 1956-1965, when leaded gasoline was introduced. The dip in the ratio toward the leaded gasoline continued in the years 1976-1985 as leaded gasoline was still being consumed. After increased regulation in the years 1996-2005, the trees were less likely to show the Pb ratios associated with leaded gasoline. This is shown in Fig 5 as the ratio starts to increase back to natural values of Pb.

The Pb in the trees is derived from gasoline residue in the soil being absorbed by the trees. The cycling of the Pb in the biosphere is a slow process, so it is expected that it will take decades for the Pb to become fully phased out of the ecosystem. The oldest samples have a $^{206}Pb/^{207}Pb$ ratio ranging from 1.193 to 2.10, indicating that these are reasonable ratios for background lead in the environment. During the use of leaded gasoline these values dipped to a minimum of 1.184, which is consistent with the 1.18-anthropogenic levels of Pb in California soils (Hurst, 1996). The $^{206}Pb/^{207}Pb$ ratio shows a shift toward these values

Table 2. Isotopic Pb ratios and concentration for tree ring samples.

SAMPLE	$^{208}Pb/^{206}Pb$	$^{207}Pb/^{206}Pb$	$^{208}Pb/^{204}Pb$	$^{207}Pb/^{204}Pb$	$^{206}Pb/^{204}Pb$	$^{206}Pb/^{207}Pb$	$^{204}Pb/^{208}Pb$	[Pb] (ppm)	pg Pb
A1	2.0901	0.84679	38.645	15.657	18.490	1.181	0.478	6.87	6874.3
A3	2.0579	0.84185	38.258	15.651	18.592	1.188	0.486	0.65	2280.1
A5	2.0642	0.84456	38.247	15.650	18.531	1.184	0.484	2.10	3143.0
A7	2.0551	0.83604	38.474	15.652	18.722	1.196	0.467	3.53	5289.2
A9	2.0344	0.82652	38.501	15.642	18.925	1.210	0.492	1.67	5182.6
B1	2.0480	0.83614	38.363	15.662	18.732	1.196	0.488	3.60	9005.8
B3	2.0563	0.84089	38.282	15.655	18.617	1.189	0.486	4.77	3340.4
B5	2.0522	0.83872	38.271	15.640	18.648	1.192	0.487	3.41	3411.1
B7	2.0467	0.83404	38.408	15.651	18.766	1.199	0.489	2.19	5039.7
B9	2.0406	0.83244	38.301	15.624	18.769	1.201	0.490	4.11	2878.1
E1	2.0621	0.84258	38.334	15.663	18.589	1.187	0.485	1.31	3808.1
E3	1.7405	0.72220	38.330	15.904	22.022	1.385	0.575	0.906	11146
E5	2.0463	0.83468	38.431	15.673	18.782	1.198	0.489	1.160	3960
E7	2.0359	0.82917	38.476	15.670	18.898	1.206	0.491	4.07	4879.4
E9	2.0378	0.82978	38.510	15.681	18.898	1.205	0.491	4.75	5229.1
H1	2.0596	0.84036	38.364	15.654	18.627	1.190	0.486	3.21	2868.6
H3	2.0504	0.83492	38.379	15.719	18.826	1.198	0.488	2.11	4015.1
H5	2.0496	0.83368	38.569	15.688	18.818	1.199	0.488	0.822	2631.4
H7	2.0405	0.83106	38.491	15.676	18.863	1.203	0.490	0.746	2611.8
H9	2.0531	0.83830	38.383	15.668	18.695	1.193	0.487	0.279	1785.8

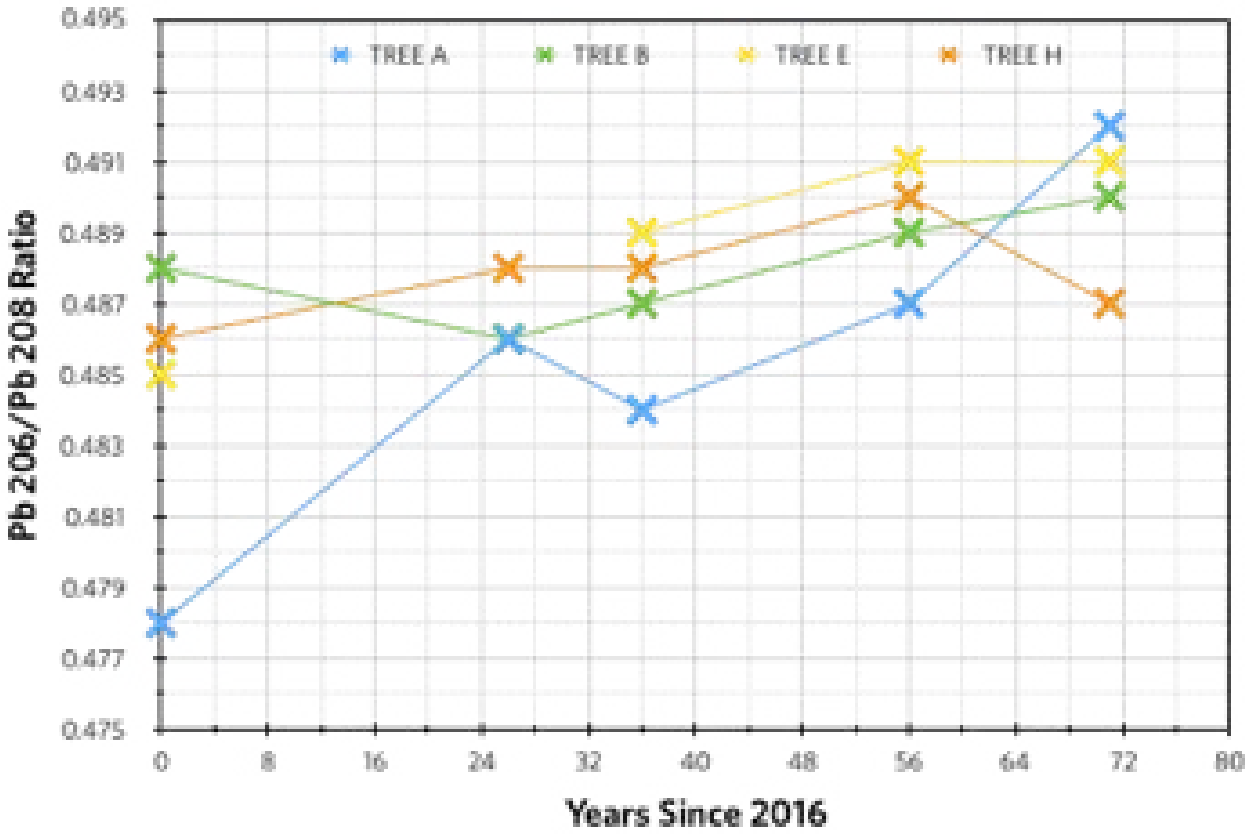

Figure 3. Plot of ratio $^{206}Pb/^{208}Pb$, shown in Table 2, for each tree against time. The ratios are plotted on the center of their ten-year time interval. Sample E3 has not been plotted because it is an anomaly. All of the trees show a monotonic decrease from time periods 1976-1985 to 1956-1965. Trees E and H show a similar trend, as they are both far from the road. Tree A and B also show a similar trend. Bark is not truly comparable to the tree ring data.

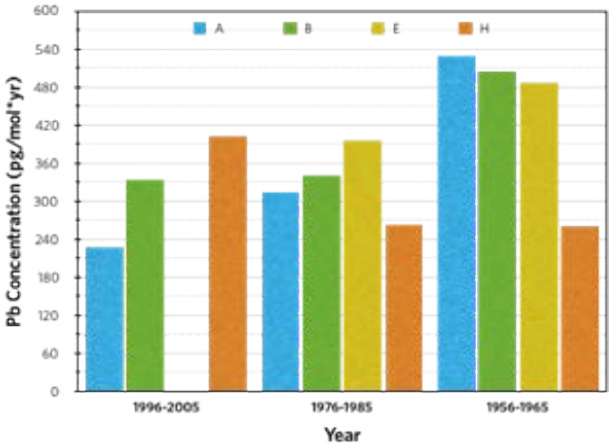

Figure 4. Graph of the Pb concentrations for each tree within its respective decade. Pb concentrations were manipulated to obtain the value for Pb (pg/mol*yr) to represent the average Pb concentration for each data set. Sample E3 has not been plotted because it is an anomaly. Tree A and Tree B show declining Pb concentrations from years 1996-2005 to years 1956-1965. Tree E shows declining Pb concentrations from the years 1976-1985 to 1956-1965. Tree H shows a substantial increase in Pb concentrations from years 1996-2005 to 1956-1965.

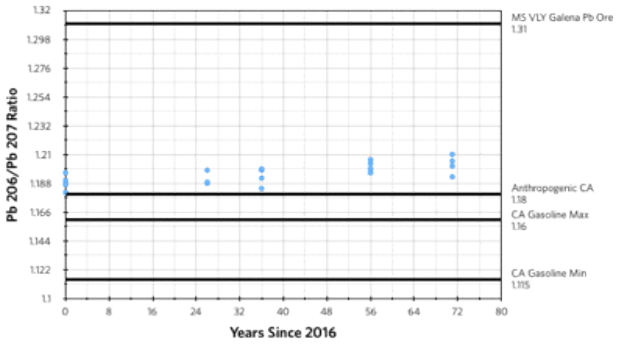

Figure 5. Graph of measured $^{206}Pb/^{207}Pb$ ratios against time. There are lines at constants referencing a sampled ratio $^{206}Pb/^{207}Pb$ for California (CA) leaded gasoline, anthropogenic soil ratio for $^{206}Pb/^{207}Pb$ in California, and value for the Mississippi Valley galena Pb ore (Hurst et al., 1996).

during and shortly following a period of common use of leaded gasoline. After increased regulation, this ratio began to return to values estimated of naturally occurring Pb. However, due to the slow nature of Pb cycling through the environment, there is still residual Pb from leaded gasoline in samples from 1996-2005.

CONCLUSION

The $^{206}Pb/^{208}Pb$ ratio shown in Fig. 3 shifts towards expected values for leaded gasoline in California during the 1960's to 1980's, during a period when leaded gasoline was poorly regulated and common. Looking at trends within approximately the past 30 years where there was increased legislation and ultimately the banning of leaded gasoline, the ratio of $^{206}Pb/^{208}Pb$ moved away from values associated with such gasoline. Trees A and B, both of which are close to the road, show a stronger influence of this trend. It is indicated that the trees closest to the road saw a stronger decreasing trend in Pb concentrations over the years than trees far from the road, which show greater variability.

ACKNOWLEDGMENTS

This research was supported by the Department of Geological Sciences at the University of North Carolina at Chapel Hill, the Anadarko Petroleum Corporation, the UNC Honors Program, the First-Year Seminar Program, the Office of Undergraduate Research Graduate Research Consultant Program and the staffs of the Sierra Nevada Aquatic Research Laboratory and Crooked Creek Station of the White Mountain Research Center. We would like to give a special thanks to Allen Glazner, Drew Coleman, John Boyd, Tyler Wickland, and Emma Blackwell for taking us to California and aiding us in our data collection in the field. Our research would not have been possible without the guidance of Connor Lawrence.

REFERENCES CITED

Agee, J.K., and Huff, M.H., 1986, The Care and Feeding of Increment Borers: Seattle, Washington, National Park Service, 15 p.

Hurst, R. W., Davis, T. E., and Chinn, B. D., 1996, The lead fingerprints of gasoline contamination: isotopic analysis of the lead additives in gasoline can improve estimates of the ages of leaks and spills: Environmental Science & Technology. v.30, p. 304A-307A.

Komarek, M., Ettler, V., Chrastny, V., and Mihaljevic, M., 2008, Lead isotopes in environmental sciences: a review, Environmental International, v. 34, p. 562-577.

Needleman, H. L., 1999, The removal of lead from gasoline: historical and personal reflections: Environmental Research, v. 84, p. 20-35, doi: 10.1006/enrs.2000.4049.

Oudijk, G., 2010, The rise and fall of organometallic additives in automotive gasoline: Environmental Forensics, v. 11, p.17-49, doi: 10.1080/15275920903346794.

Phipps, R.L., and McGowan, J., 1993, Tree rings: timekeepers of the past: Denver, Colorado, U.S. Department of the Interior, 15 p.

Sawyer, R. F., 1993, Trends in auto emissions and gasoline composition: Environmental Health Perspectives, v. 101, p. 5-12.

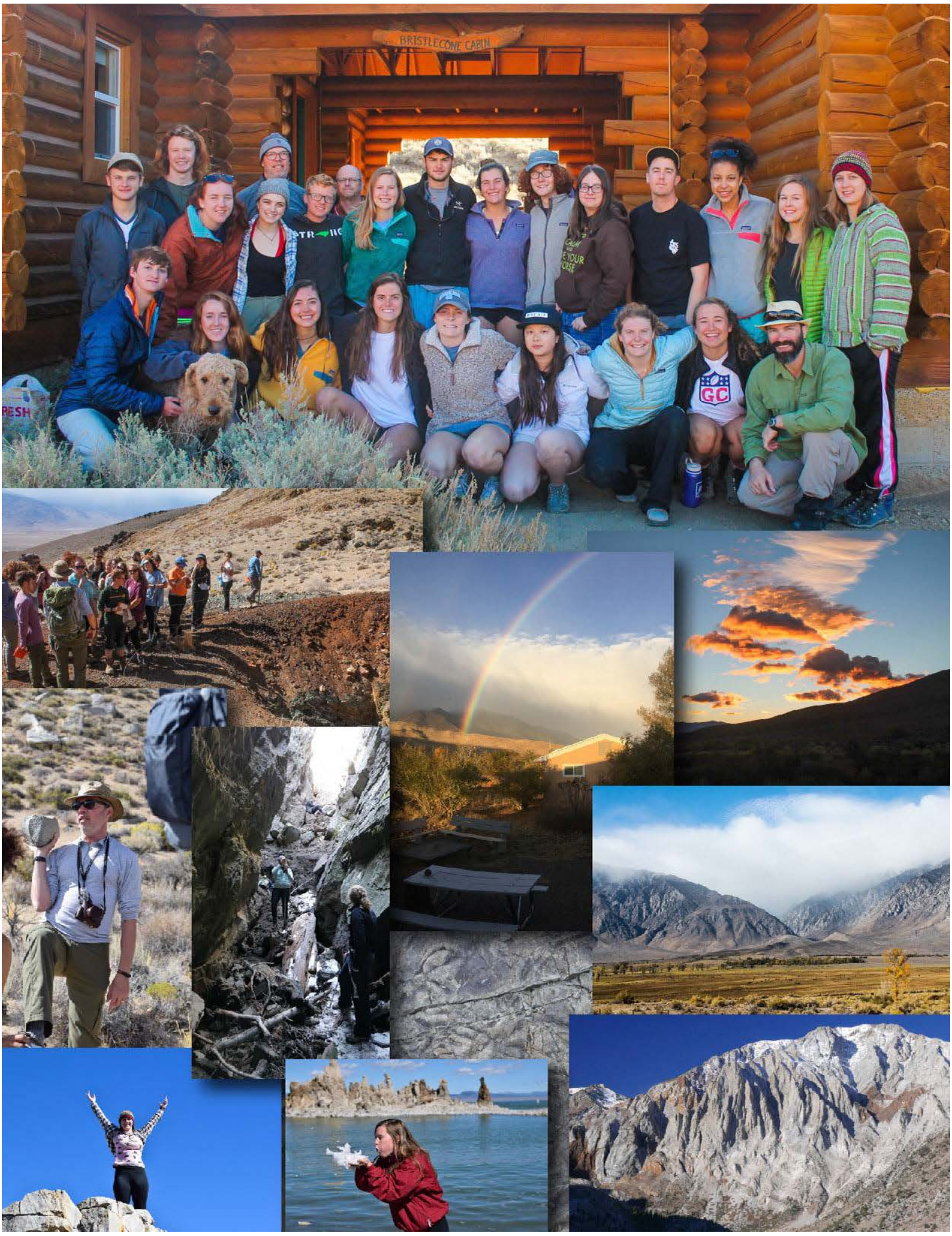
BRISTLECONE CABIN
GC